

Full length article

Interfacial nanophases stabilize nanotwins in high-entropy alloys

Wenjun Lu^a, Christian H. Liebscher^a, Fengkai Yan^a, Xufei Fang^{a,b}, Linlin Li^a, Jianjun Li^c,
Wenqi Guo^a, Gerhard Dehm^a, Dierk Raabe^a, Zhiming Li^{a,d,*}

^a Max-Planck-Institut für Eisenforschung, Max-Planck-Straße 1, 40237, Düsseldorf, Germany

^b Institute of Materials Science, Technische Universität Darmstadt, D-64287, Germany

^c College of Mechanical and Electrical Engineering, Central South University, Changsha, 410083, China

^d School of Materials Science and Engineering, Central South University, Changsha 410083, China



ARTICLE INFO

Article history:

Received 2 October 2019

Revised 3 December 2019

Accepted 4 December 2019

Available online 7 December 2019

Key words:

Nanotwins

Thermal stability

Elongated $M_{23}C_6$

9R structure

High entropy alloy

ABSTRACT

Nanostructuring metals through nanograins and nanotwins is an efficient strategy for strength increase as the mean free path of dislocations is reduced. Yet, nanostructures are thermally often not stable, so that the material properties deteriorate upon processing or during service. Here, we introduce a new strategy to stabilize nanotwins by an interfacial nanophase design and realize it in an interstitial high-entropy alloy (iHEA). We show that nanotwins in a carbon-containing FeMnCoCrNi iHEA can remain stable up to 900 °C. This is enabled by co-segregation of Cr and C to nanoscale 9R structures adjacent to incoherent nanotwin boundaries, transforming the 9R structures into elongated nano-carbides in equilibrium with the nanotwin boundaries. This nanoscale 9R structures assisted nano-carbide formation leads to an unprecedented thermal stability of nanotwins, enabling excellent combination of yield strength (~1.1 GPa) and ductility (~21%) after exposure to high temperature. Stimulating the formation of nano-sized 9R phases by deformation together with interstitial doping establishes a novel interfacial-nanophase design strategy. The resulting formation of nano-carbides at twin boundaries enables the development of strong, ductile and thermally stable bulk nanotwinned materials.

© 2019 Acta Materialia Inc. Published by Elsevier Ltd. All rights reserved.

1. Introduction

Strength, ductility and thermal stability are key properties of metallic materials applied in such diverse fields as safe infrastructures, weight reduced automobiles and efficient energy conversion plants. Improving the strength of metals by refining their grain size down to the nanoscale (<100 nm) often results in insufficient thermal stability, a challenge known as strength-stability trade-off for nanocrystalline materials [1,2]. Loss of nanosized substructures is due to capillary-driven boundary migration-induced crystal coarsening (e.g., at ~445 °C in nanocrystalline Ni) [1]. Previous efforts for solving this strength-stability trade-off mainly focused on the introduction of more stable planar defects such as nanoscale coherent twin boundaries (nanotwins) [1,3]. However, twin boundaries get thermally unstable at ~500 °C for instance in nanotwinned Ni [1], ~745 °C in nanotwinned 316 L stainless steels [4], and ~680 °C in nanotwinned Fe-Cr based superalloys [5]. As twin interfaces have high lattice site coincidence their energy is very low [6–9], so that their stabilization through Zener-type particle

pinning is ineffective [7,10–12]. Thus, a mechanism for stabilizing twin interfaces at elevated temperatures, as a vehicle for realizing high strength and ductility of materials exposed to harsh thermal conditions, is missing.

In this context the interfacial nanophase design concept developed in the presented study offers a suited option. We apply this approach and show how nanophases can stabilize nanotwins in an interstitial high-entropy alloy (iHEA).

Our starting point for this interfacial nanophase design approach is the nanoscale 9R structure that has been reported to occur as transformation zone at certain planar defects [13–16]. More specific, incoherent portions of twin boundaries can be generated from coherent ones through partial dislocation reactions [7]. In such regions hexagonal 9R structures can form. They consist of a specific stacking sequence of {111} atomic planes in the order ABC/BCA/CAB, where each letter indicates one of the three possible stacking positions. The core structure of the incoherent twin boundary can be described as a repeatable sequence of Shockley partial dislocations $b_2:b_1:b_3$. b_1 is a pure edge partial dislocation, which is equal to $1/6[11\bar{2}]$; b_2 and b_3 are mixed partial dislocations with opposite sign of their screw portions, which are equal to $1/6[2\bar{1}1]$ and $1/6[1\bar{2}1]$, respectively [15,17,18]. The atomic stacking of the 9R structure is created by the emission

* Corresponding author at: School of Materials Science and Engineering, Central South University, Changsha 410083, China.

E-mail address: zhiming.li@mpie.de (Z. Li).

and passage of Shockley partial dislocations. The preferred partial dislocation emitted is b_1 , since b_2 and b_3 attract each other due to the opposite sign of their screw components. In this way, the 9R structure is bounded by two phase boundaries, i.e., PB_1 , containing Shockley partials b_1 , and PB_2 , which is composed of an array of b_2 and b_3 dislocations at the location of the original incoherent twin boundary [17–19]. In such a scenario, the 9R structure is thermodynamically stabilized by the presence of defects, although the structure itself would be unstable. Owing to its inherent high dislocation density at both PB_1 and PB_2 , the local mismatch across the 9R bounding interface promotes local elemental diffusion and element enrichment, leading to Gibbs-type equilibrium segregation and possible transformation reactions at such interfaces [17,20].

Inspired by these ideas we demonstrate here a novel strategy of utilizing the interfacial nanophase design concept for the stabilization of nanotwins in an iHEA containing multiple principal substitutional elements (e.g., Co, Cr, Fe, Mn and Ni) and interstitial carbon. The formation of nanophases at planar defects – here the 9R structures at incoherent twin boundaries – in an iHEA takes place during cold rolling and assists nano-carbide formation by subsequent high-temperature annealing, rendering nanotwins thermally stable.

2. Materials and methods

2.1. Materials preparation

The ingots of the $Fe_{19.84}Mn_{19.84}Co_{19.84}Cr_{19.84}Ni_{19.84}C_{0.8}$ (at.%) iHEA and the $Fe_{20}Mn_{20}Co_{20}Cr_{20}Ni_{20}$ (at.%) equiatomic HEA were cast in a vacuum induction furnace using pure metals and carbon ($\geq 99.8\%$ pure). Both ingots had dimensions of $25 \times 60 \times 65 \text{ mm}^3$ with a weight of 1 kg. Blocks with dimensions of $10 \times 25 \times 60 \text{ mm}^3$ were machined from the original casts, and subsequently hot-rolled at 950°C to a thickness reduction of 50% (thickness changed from 10 to 5 mm). The hot-rolled alloy plates were homogenized at 1200°C for 2 h in Ar atmosphere followed by water-quenching. After that, the alloy plates were further cold-rolled with a thickness reduction of 60% and then annealed at 800°C for 10–600 min and 900°C for 10–60 min in Ar atmosphere followed by water-quenching.

2.2. Mechanical and microstructural characterization

Nanoindentation measurements were performed at room temperature using G200 (Keysight-Tec, USA) for all annealed samples. A diamond Berkovich indenter was used at a constant loading rate (0.05 s^{-1}) up to a maximum displacement of 500 nm. This depth was chosen as a compromise to exclude the indentation size effect on the one hand and to ensure a sufficient number of indents in a small local region on the other hand to provide sufficient statistics for the hardness evaluation. The nanohardness analysis was calculated based on the Oliver-Pharr method [21].

For room-temperature tensile tests, flat specimens with a thickness of 1 mm were machined from the alloy sheets by electrical discharge machining. The gauge length and width of the tensile specimens were 10 mm and 2.5 mm, respectively. Uniaxial tensile testing was carried out at ambient temperature using a Kammrath & Weiss tensile stage at an initial strain rate of $1 \times 10^{-3} \text{ s}^{-1}$. The local strain values were determined by digital image correlation (DIC) method using the Aramis system. For high-temperature tensile tests, flat dog-bone-shaped specimens with a thickness of 1 mm were machined from the cold-rolled alloy plates. The gauge length and width of the specimens were 100 and 25 mm, respectively. High-temperature uniaxial tensile testing was conducted at 600°C and 700°C with an initial engineering strain rate of

$1 \times 10^{-3} \text{ s}^{-1}$ using a Gleeble 3500 thermomechanical simulator. Before the start of the high-temperature straining, the samples were held for 15 min after reaching the desired test temperature.

The microstructures of the bulk samples prior to and after annealing were characterized using multiple probing techniques. The sample surface was mechanically grinded with silicon carbide abrasive paper (P60 to P4000), and then polished by using 3–1 μm diamond suspensions. Final polishing with $\sim 50 \text{ nm}$ SiO_2 suspension was carried out to remove the deformation layer caused by mechanical grinding. X-ray diffraction (XRD) analysis was performed using an X-ray instrument ISO-DEBYEFLEX 2003 equipped with $\text{Co K}\alpha$ ($\lambda = 1.788965 \text{ \AA}$) source at 40 kV and 30 mA. Electron channeling contrast imaging (ECCI) and transmission Kikuchi diffraction (TKD) analysis were conducted on a Zeiss-Merlin microscope at 20 kV. Electron backscatter diffraction (EBSD) was carried out by a Zeiss-crossbeam FIB scanning electron microscope (SEM) with TSL OIM detector using 100 nm step size at 15 kV. The transmission electron microscope (TEM) foils and atom probe tomography (APT) tips were prepared by a dual-beam focus ion beam (FIB FEI 600i instrument) via TEM lift-out procedures [22] and APT lift-out procedures [23], respectively. Bright-field TEM, dark-field TEM and selected area electron diffraction (SAED) were conducted by an image aberration-corrected TEM (FEI Titan Themis) at an acceleration voltage of 300 kV. High-resolution high angle annular dark field (HAADF) scanning TEM (STEM), low angle annular dark field (LAADF) STEM and energy dispersive X-ray spectroscopy (EDS) were carried out by means of a probe aberration-corrected TEM/STEM (FEI Titan Themis) with an acceleration voltage of 300 kV. For HAADF-STEM imaging, a probe semi-convergence angle of 17 mrad and inner and outer semi-collection angles ranging from 73 to 200 mrad were operated. For LAADF-STEM imaging, a probe semi-convergence angle of 17 mrad and inner and outer semi-collection angles from 14 to 63 mrad were utilized. For *in-situ* STEM investigation, the samples were heated using a Lighting heating/biasing holder from DENSolutions (Delft, Netherlands). A heating rate of approximately 100°C/s was applied up to 900°C . All crystallographic analyses were assisted by comparing the observed patterns to simulated electron diffraction patterns and the corresponding stereographic analysis using electron microscopy simulation software (Crystallmaker) under an assumption of a 100 nm TEM foil/lamella thickness and an acceleration voltage of 300 kV. The crystallographic information (CIF files) of face-centered cubic (FCC) γ matrix and $M_{23}C_6$ carbide were taken from Refs. [24,25]. APT measurements were conducted by using a LEAP 3000X HR instrument (Cameca company) operated in voltage mode with 200 kHz pulse repetition rate, 15% pulse fraction, 0.5% detection rate and a set-point temperature of 70 K. APT tip reconstruction and data analysis were conducted by the IVAS 3.6.12 software.

3. Results and discussion

3.1. Microstructure evolution upon high temperature annealing

We produced an iHEA with nominal composition $Fe_{19.84}Mn_{19.84}Co_{19.84}Cr_{19.84}Ni_{19.84}C_{0.8}$ (at.%) as a model material for realizing the interfacial nanophase design concept. For reference, an equiatomic FeMnCoCrNi HEA without carbon addition has also been prepared and investigated after imposing it to the same processing steps. Both, the equiatomic FeMnCoCrNi HEA and the carbon doped iHEA in as-homogenized conditions were processed by cold-rolling and subsequent annealing at 900°C and 800°C for various times. Fig. 1a and b show the microstructures of the equiatomic FeMnCoCrNi reference HEA prior to and after $900^\circ\text{C}/10 \text{ min}$ annealing, respectively. All nanotwins ($\sim 53 \text{ nm}$ in thickness) and deformation bands ($\sim 18 \text{ vol.}\%$) in the cold-rolled

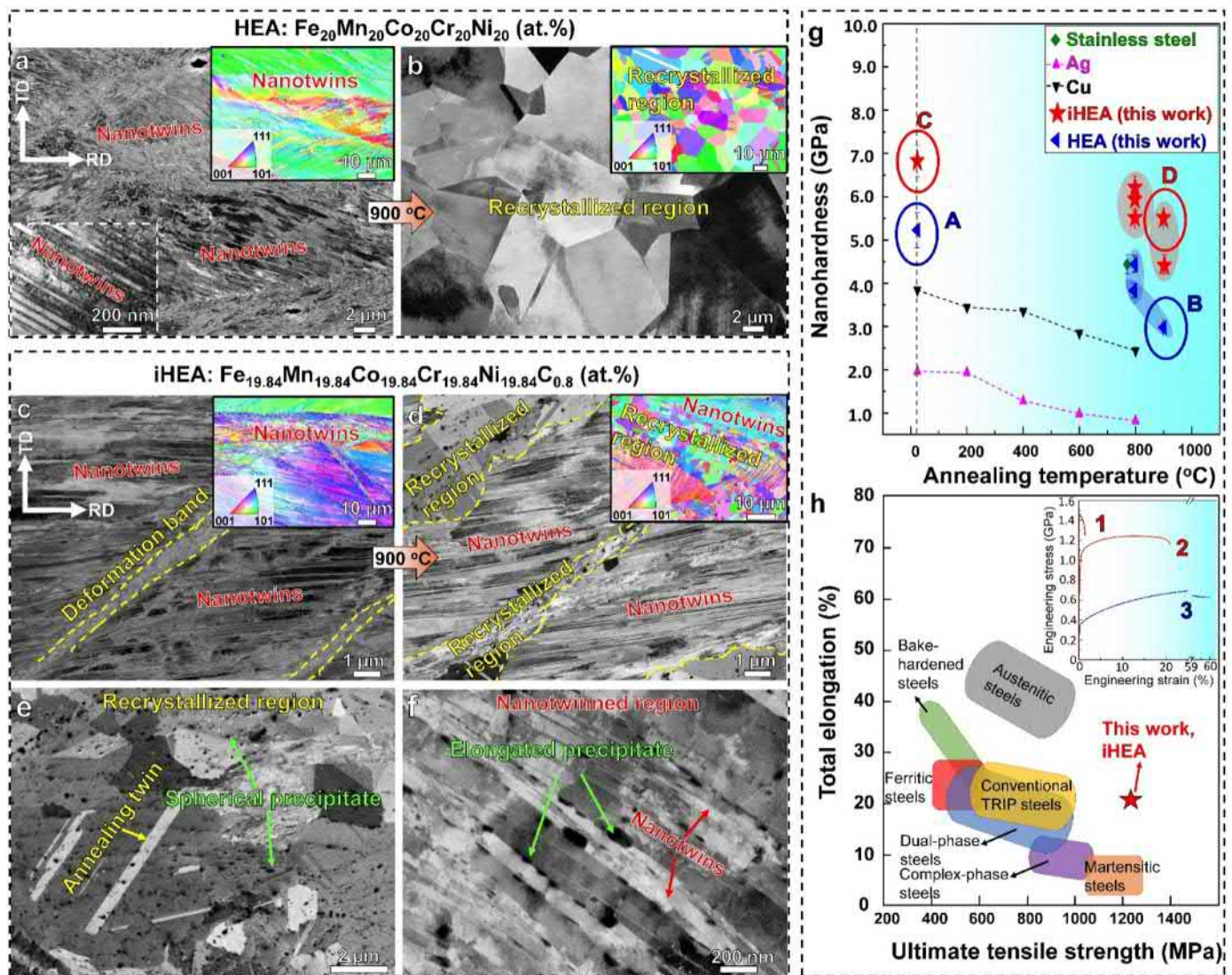


Fig. 1. Microstructure and mechanical properties of the equiatomic FeMnCoCrNi HEA and the iHEA prior to and after annealing. (a) ECC image of cold-rolled microstructure of the equiatomic HEA. (b) Fully recrystallized structure of the equiatomic HEA after annealing at 900 °C for 10 min. (c) Cold-rolled microstructure of the iHEA. (d) Partially recrystallized structure of the iHEA after annealing at 900 °C for 10 min. The insets in (a–d) are corresponding EBSD orientation maps. (e) Microstructure of the recrystallized region with spherical precipitates. (f) Microstructure of the nanotwinned region with elongated precipitates. (g) Nanoindentation hardness of the nanotwinned iHEAs in different states (e.g., cold-rolled, 800 °C/10 min, 800 °C/30 min, 900 °C/10 min and 900 °C/60 min annealed) compared with those of other existing nanotwinned metallic materials including nanotwinned FeMnCoCrNi HEA in different states (e.g., cold-rolled, 800 °C/10 min, 800 °C/30 min and 900 °C/10 min annealed), nanotwinned 316 L stainless steel (SS) (780 °C/20 min) [29], nanotwinned Ag (23–800 °C/1 h) [30] and nanotwinned Cu (23–800 °C/1 h) [31]. Annealing temperature of 23 °C refers to the cold-rolled state of the sample without annealing. The additional results showing the microstructure and high-temperature tensile properties of the iHEA and HEA after heat treatments for extended times can be found in Figs. 6, 7 and 12. (h) Comparison of mechanical properties of the nanotwinned iHEA with other materials. The inset in (h) is engineering stress-strain curves of the annealed HEA (curve 3), the cold-rolled (curve 1) and the annealed (curve 2) iHEAs. “RD” and “TD” refer to rolling and transverse directions, respectively.

microstructure (Fig. 1a) were completely removed by recrystallization, leaving only coarse equiaxed grains ($\sim 4.4 \mu\text{m}$) after annealing (Fig. 1b). No secondary phases were found in the fully recrystallized HEA (Fig. 1b). Compared to the equiatomic FeMnCoCrNi reference HEA (Fig. 1a), the cold-rolled iHEA presents a similar microstructure containing dislocations ($> 10^{15} \text{ m}^{-2}$), nanotwins ($\sim 40 \text{ nm}$ in thickness) and deformation bands ($\sim 12 \text{ vol.}\%$) (Fig. 1c). Unlike the annealed equiatomic FeMnCoCrNi HEA (Fig. 1b), the annealed iHEA exhibits a heterogeneous microstructure consisting of recrystallized ($\sim 40 \text{ vol.}\%$) and non-recrystallized ($\sim 60 \text{ vol.}\%$) regions (Fig. 1d). The non-recrystallized region contains a high number density of nanotwins which are $\sim 100 \text{ nm}$ in width. ECCI reveals that the recrystallized region with equiaxed grains of $\sim 2 \mu\text{m}$ contains spherically shaped precipitates with an average size of $\sim 150 \text{ nm}$ (Fig. 1e), whereas the nanotwinned non-recrystallized region contains precipitate with elongated shape ($\sim 30 \text{ nm}$ in

width) arranged along the nanotwin interfaces (Fig. 1f). Such types of heterogeneous microstructures usually enable balanced strength and ductility at room temperature [26], which is often associated with a high density of interfaces [27].

We next analyze how the nanotwins can prevail in the iHEA even when exposed to high temperatures. Typical ECCI analysis (Fig. 1e and f) reveals two types of nano-precipitates in the iHEA after 900 °C/10 min annealing in terms of morphology and size. Smaller elongated precipitate ($\sim 30 \text{ nm}$ in width) have formed along certain portions of the nanotwin boundaries in the nanotwinned zones. In contrast, spherical precipitates with larger size ($\sim 150 \text{ nm}$) are distributed homogeneously both, in the grain interiors and at the grain boundaries in the recrystallized regions. We analyzed the elongated precipitates first by using a combination of TEM (Fig. 2a–c), HAADF-STEM (Fig. 2d) and EDS (Fig. 2e). The results show that these elongated interfacial zones are face-

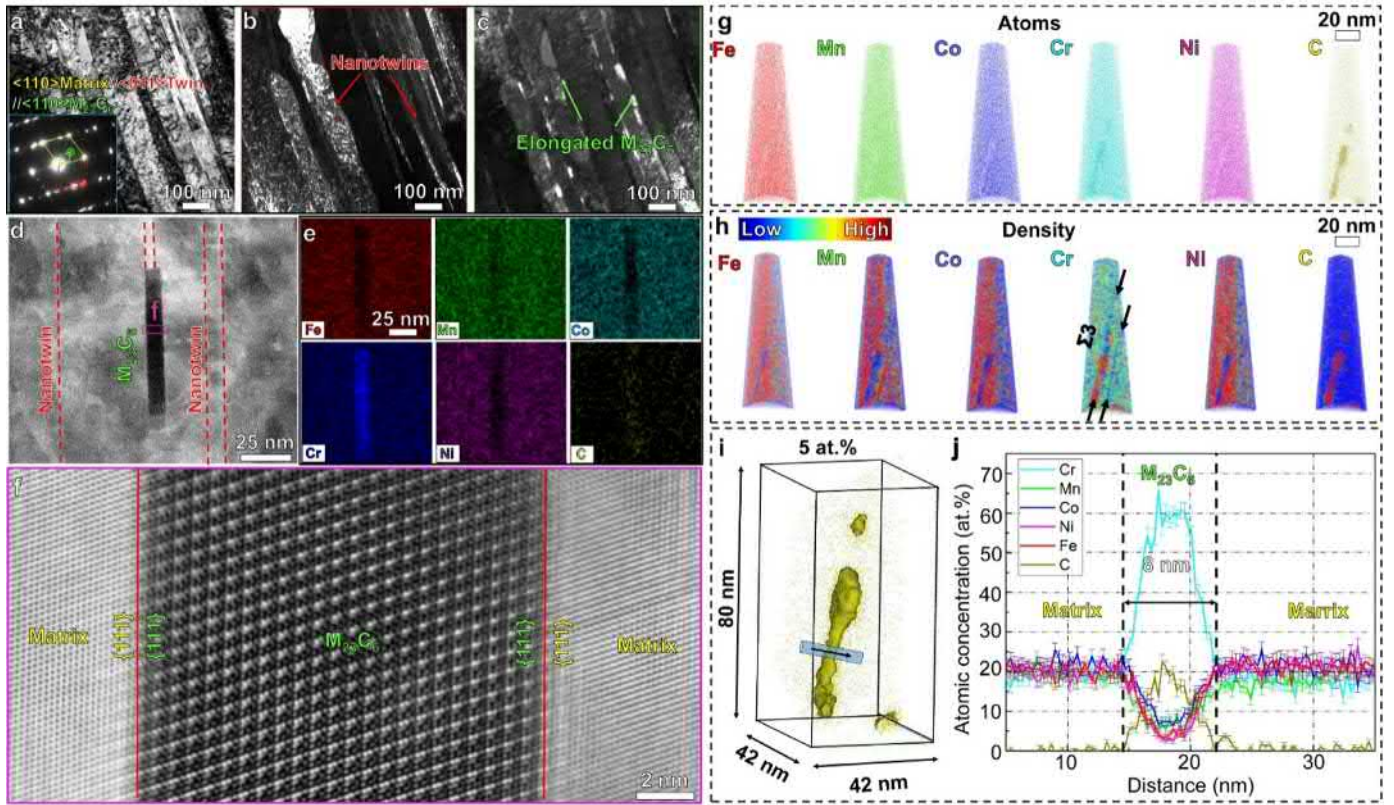


Fig. 2. Typical TEM-STEM-APT analysis of the nanotwinned region of the iHEA after annealing. (a) Linear substructures in the nanotwinned region. The inset is a corresponding SAED pattern. (b) Dark-field TEM images taken by a twin reflection (red circle in (a)). (c) Dark-field TEM images taken by a superlattice reflection of the precipitates (green circle in (a)). The inset SAED pattern shows a cube-on-cube orientation relationship between the elongated precipitate and the FCC γ matrix. (d) HAADF-STEM image of the elongated precipitate along nanotwin boundaries. (e) The corresponding STEM-EDS maps. (f) Atomic structure of the elongated $M_{23}C_6$ (M: Fe, Mn, Co, Ni, Cr) by high-resolution STEM from the region marked in (d) revealing the orientation relationship between matrix and precipitate: $\langle 110 \rangle_{\text{matrix}} // \langle 110 \rangle_{\text{precipitate}}$ and $\{111\}_{\text{matrix}} // \{111\}_{\text{precipitate}}$. (g) 3D atom maps of Fe, Mn, Co, Cr, Ni and C in a typical tip containing elongated precipitate. (h) Blue-to-red rainbow color density maps of Fe, Mn, Co, Cr, Ni and C, in which blue and red indicate the lowest and highest atomic densities, respectively. Planar features of the decreased Cr density indicate the positions of nanotwin boundaries (marked by black arrows). (i) 3D carbon atom map with isocomposition surface of 5 at.% C (yellow). (j) 1D compositional profile within the cylinder ($5 \times 5 \times 35$ nm) highlighted in (i) along the direction marked with the black arrow. (For interpretation of the references to colour in this figure legend, the reader is referred to the web version of this article.)

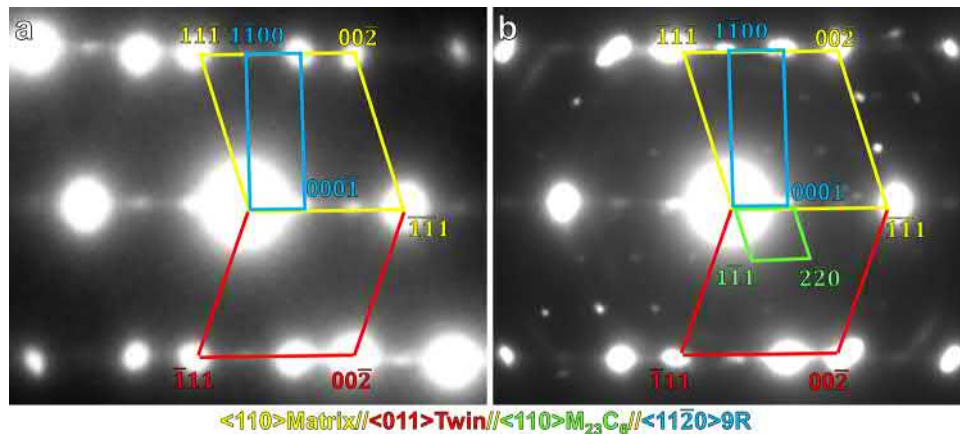


Fig. 3. SAED analysis of the 9R structure. (a) Without nano-carbide; (b) With nano-carbide.

centered cubic (FCC) structured nano-carbides enriched in Cr [25]. We probed them by high-resolution HAADF-STEM (Fig. 2f) and found an orientation relationship between these carbide regions and the adjacent nanotwinned matrix of $\langle 110 \rangle_{\text{matrix}} // \langle 110 \rangle_{\text{carbide}}$ and $\{111\}_{\text{matrix}} // \{111\}_{\text{carbide}}$ [28–30] (Fig. 3). APT analysis (Fig. 2g–h) confirms that they are $M_{23}C_6$ (M: Fe, Mn, Co, Ni, Cr) nano-carbides, with a C concentration of ~20.5 at.%.

We next analyzed the spherical precipitates in the recrystallized regions by TEM (Fig. 4a and c), SAED (Fig. 4b), HAADF-

STEM (Fig. 4d), TKD (Fig. 4d), and EDS (Fig. 4e). We found that they are also FCC structured nano-carbides enriched in Cr [25]. The orientation relationship between these spherical nano-carbides and the recrystallized matrix was determined to be $\langle 110 \rangle_{\text{matrix}} // \langle 110 \rangle_{\text{carbide}}$ and $\{111\}_{\text{matrix}} // \{111\}_{\text{carbide}}$ [28–30] by high-resolution STEM (Fig. 4f). APT (Fig. 4g–j) measurements further reveal that their chemical composition of $(Cr_{0.76}Co_{0.09}Mn_{0.07}Fe_{0.05}Ni_{0.03})_{23}C_6$ (at.%) also matches that of the $M_{23}C_6$ prototype structure and is identical to that

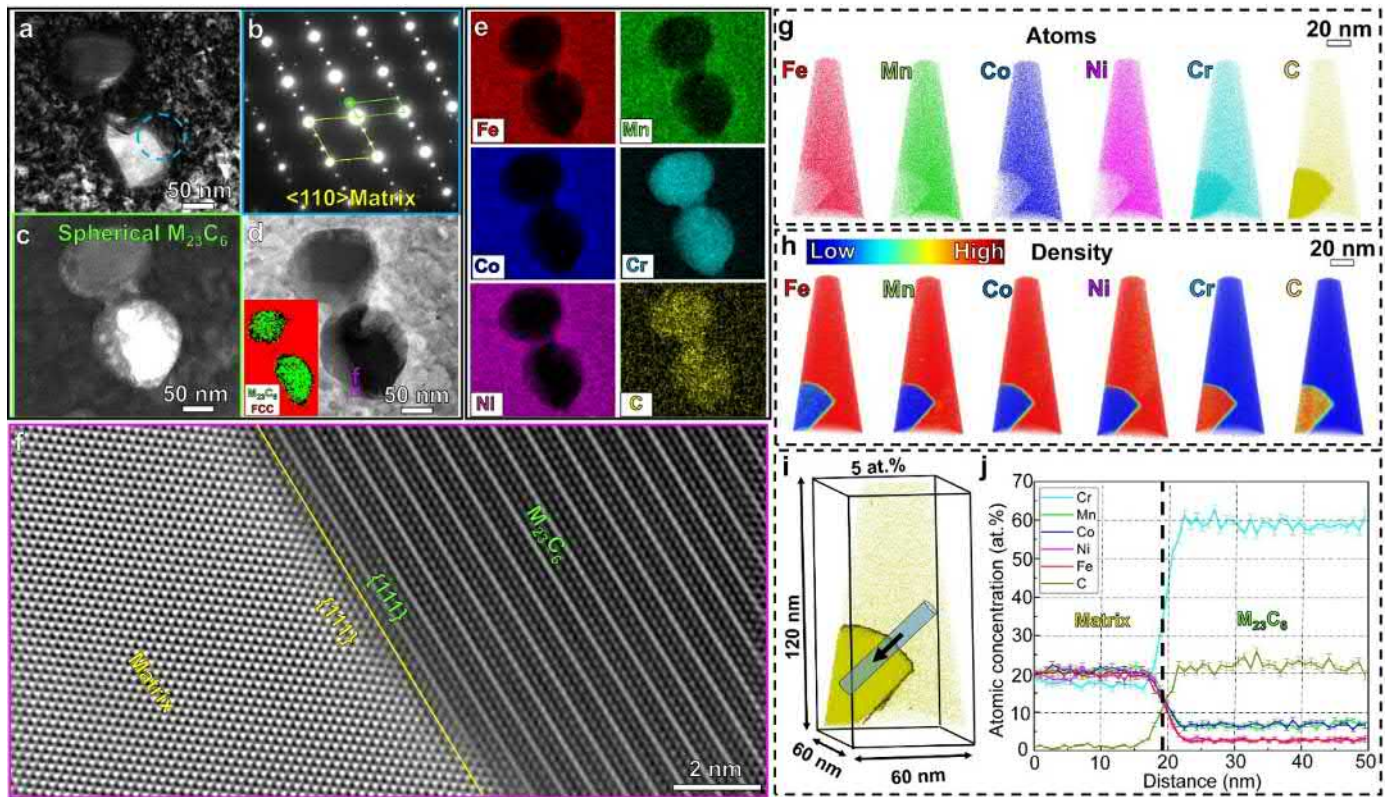


Fig. 4. Typical TEM-STEM-APT analysis of the recrystallized region of the iHEA after annealing. Typical spherical precipitates are characterized by (a) bright-field TEM imaging, (b) selected area electron diffraction (SAED) generated from the region (blue dashed circle) marked in (a). (c) Dark-field TEM image taken by the diffraction reflection marked by the green circle in (b). (d) HAADF-STEM image with the corresponding inset TKD map. (e) STEM-EDS maps of the sample region in (d). (f) High-resolution STEM image of the squared region in the spherical precipitates in (d) confirming the orientation relationship between the matrix and the precipitate is $\langle 110 \rangle_{\text{matrix}} // \langle 110 \rangle_{\text{precipitate}}$ and $\{111\}_{\text{matrix}} // \{111\}_{\text{precipitate}}$. (g) 3D atom maps of Fe, Mn, Co, Cr Ni and C in a typical tip containing a spherical precipitate. (h) Blue-to-red rainbow color density maps of Fe, Mn, Co, Cr Ni and C corresponding to the atom maps in (g); blue indicates the lowest atomic density and red presents the highest atomic density. (i) 3D carbon atom map with isocomposition surface of 5 at.% C (yellow). (j) 1D compositional profile within the cylinder ($10 \times 10 \times 50$ nm) highlighted in (i) along the direction marked with the black arrow. (For interpretation of the references to colour in this figure legend, the reader is referred to the web version of this article.)

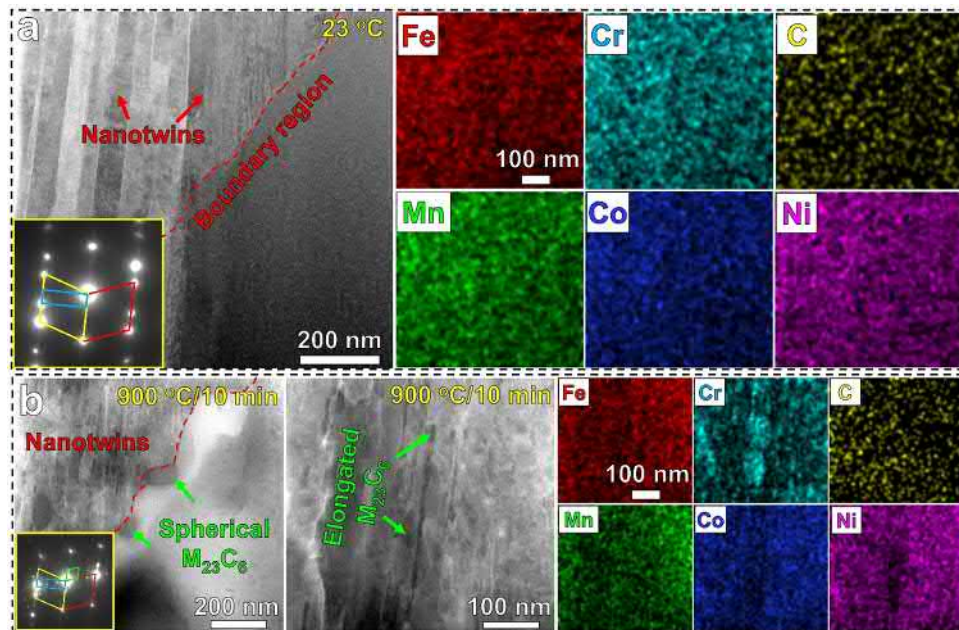


Fig. 5. *In-situ* heating conducted under HAADF-STEM mode illustrating the formation of $M_{23}C_6$ carbides within the nanotwinned iHEA. (a) HAADF-STEM image and EDS maps for the cold-rolled iHEA prior to *in-situ* heating; (b) HAADF-STEM image and EDS maps for the iHEA after *in-situ* heating at 900 °C for 10 min. The insets are SAEDs showing the presence of the matrix, nanotwins, 9R structures and $M_{23}C_6$ carbides.

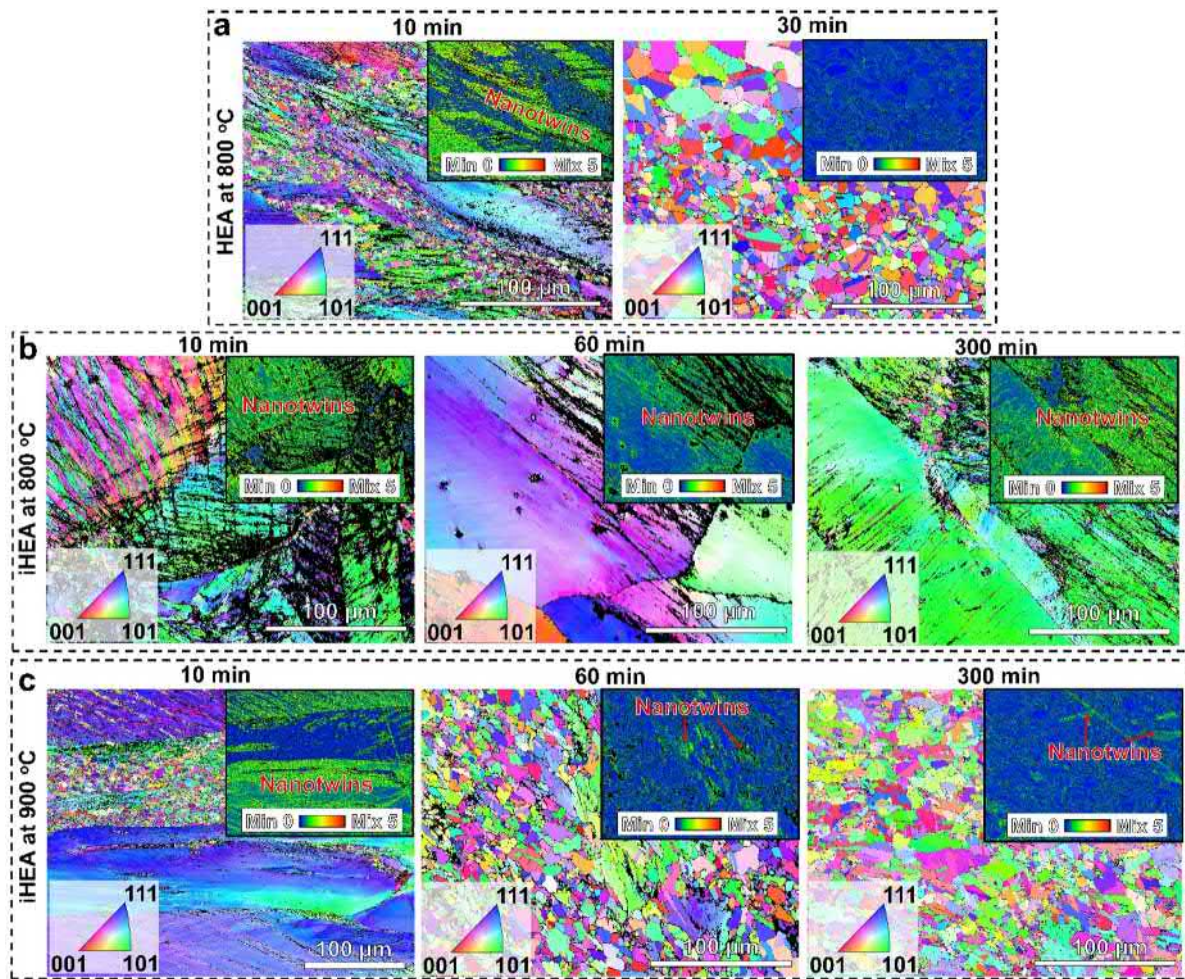


Fig. 6. Thermal stability with extended annealing times. Typical EBSD inverse pole figure (IPF) maps and Kernel average misorientation (KAM) maps of samples annealed at high temperatures for various time periods. (a) HEAs annealed at 800 °C for 10 and 30 min. (b) iHEAs annealed at 800 °C for 10, 60 and 300 min. (c) iHEAs annealed at 900 °C for 10, 60 and 300 min.

of the elongated nano-carbides analyzed in the nanotwinned regions.

We further utilized *in-situ* heating in HAADF-STEM mode in conjunction with EDS to explore the formation of these precipitates including the elongated and spherical carbides in the nanotwinned iHEA, as displayed in Fig. 5. We observe a high density of nanotwins in the cold-rolled iHEA prior to *in-situ* heating (Fig. 5a). Heating at 900 °C for 10 min leads to formation of spherical $M_{23}C_6$ carbides at the grain boundaries and precipitation of elongated $M_{23}C_6$ carbides along the nanotwin boundaries (Fig. 5b). We also find that the nanotwins can even be stabilized for extended time intervals at elevated temperatures as shown by data obtained after 800 °C/60 min, 800 °C/300 min and 900 °C/60 min *ex-situ* heating cycles (Figs. 6 and 7), revealed by EBSD mapping and a corresponding kernel average misorientation (KAM) analysis.

3.2. Nanoindentation analysis

Fig. 1g shows the hardness values of the nanotwin-containing iHEAs after annealing at 900 °C and 800 °C for various times. The nanoindentation hardness distribution map and the corresponding microstructure of the probed region for the sample exposed to a 900 °C/10 min annealing treatment are displayed in Figs. 8 and 9 as reference state. To correlate the microstructure differences with hardness, systematic nanoindentation probing with 150 nanoindentations were conducted on an area (900 °C for 10 min) containing both the nanotwinned and the recrystallized regions, for obtain-

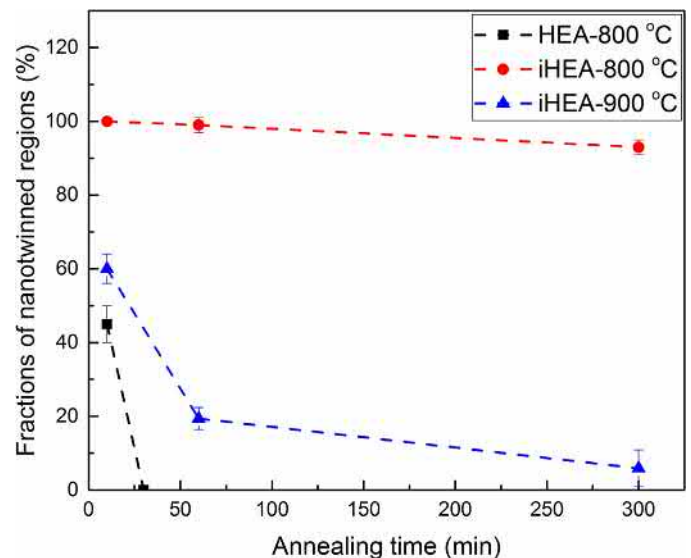


Fig. 7. Fractions of nanotwinned regions as a function of annealing time for both HEA and iHEA.

ing statistically representative data sets. As shown in Fig. 8a–c, the nanoindentations were placed with a spacing of ~12 μm in order to avoid overlap of the associated plastic zones [31]. Fig. 8d shows

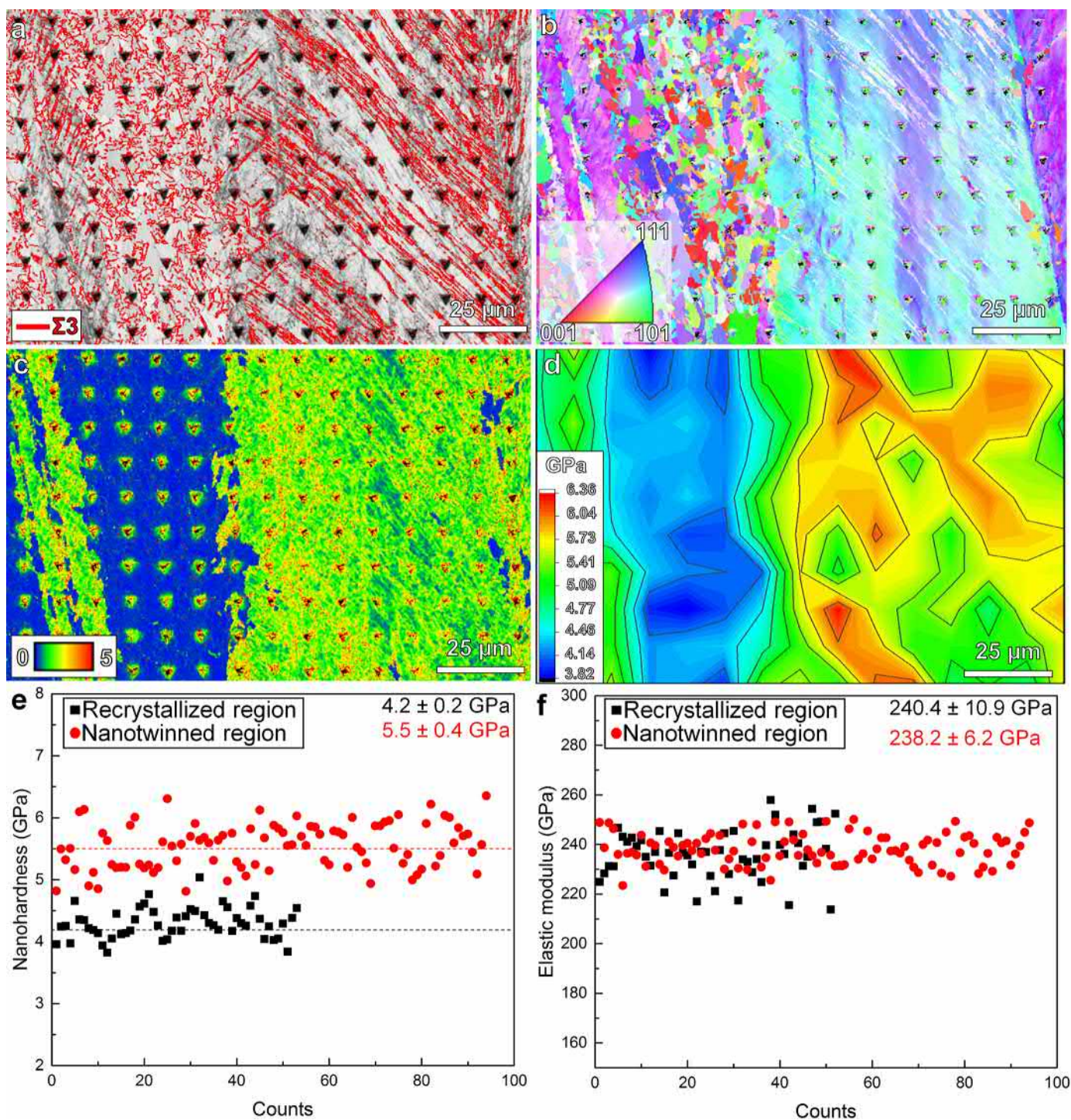


Fig. 8. Nanoindentation analysis of the iHEA annealed at 900 °C for 10 min. Typical EBSD maps of (a) grain boundaries, (b) inverse pole figure and (c) KAM for a microstructure containing both the recrystallized and the nanotwinned regions. (d) is the corresponding hardness distribution map of the same area. (e) and (f) are statistical distribution of nanohardness and elastic modulus for both the recrystallized and nanotwinned regions. “Σ3” in (a) refers to twin boundaries.

a typical nanohardness distribution map of the same sample area in Fig. 8a–c. The nanohardness of the nanotwinned region is remarkably higher compared to that of the recrystallized region. In order to quantitatively compare the micromechanical properties of the iHEA, both the nanohardness and the elastic modulus of the nanotwinned and the recrystallized regions were analyzed according to the Oliver-Pharr method [21]. As presented in Fig. 8e, the nanohardness of the nanotwinned region is in a range from ~5.0 to ~6.0 GPa, and the average value is 5.5 ± 0.4 GPa, which is ~1.3 GPa

higher than that of the recrystallized region (average value of 4.2 ± 0.2 GPa). Unlike the nanohardness value, the average elastic modulus of the nanotwinned region (238.2 ± 6.2 GPa) is almost identical to that of the recrystallized region (240.4 ± 10.9 GPa), as displayed in Fig. 8f. This is due to the fact that nanotwins do not affect the elastic properties of the matrix grains [31].

Fig. 9a shows the overview ECC image of the nanoindentation area. ECCI and EBSD analysis of two typical indents (positions 1 and 2) from the recrystallized and nanotwinned regions were per-

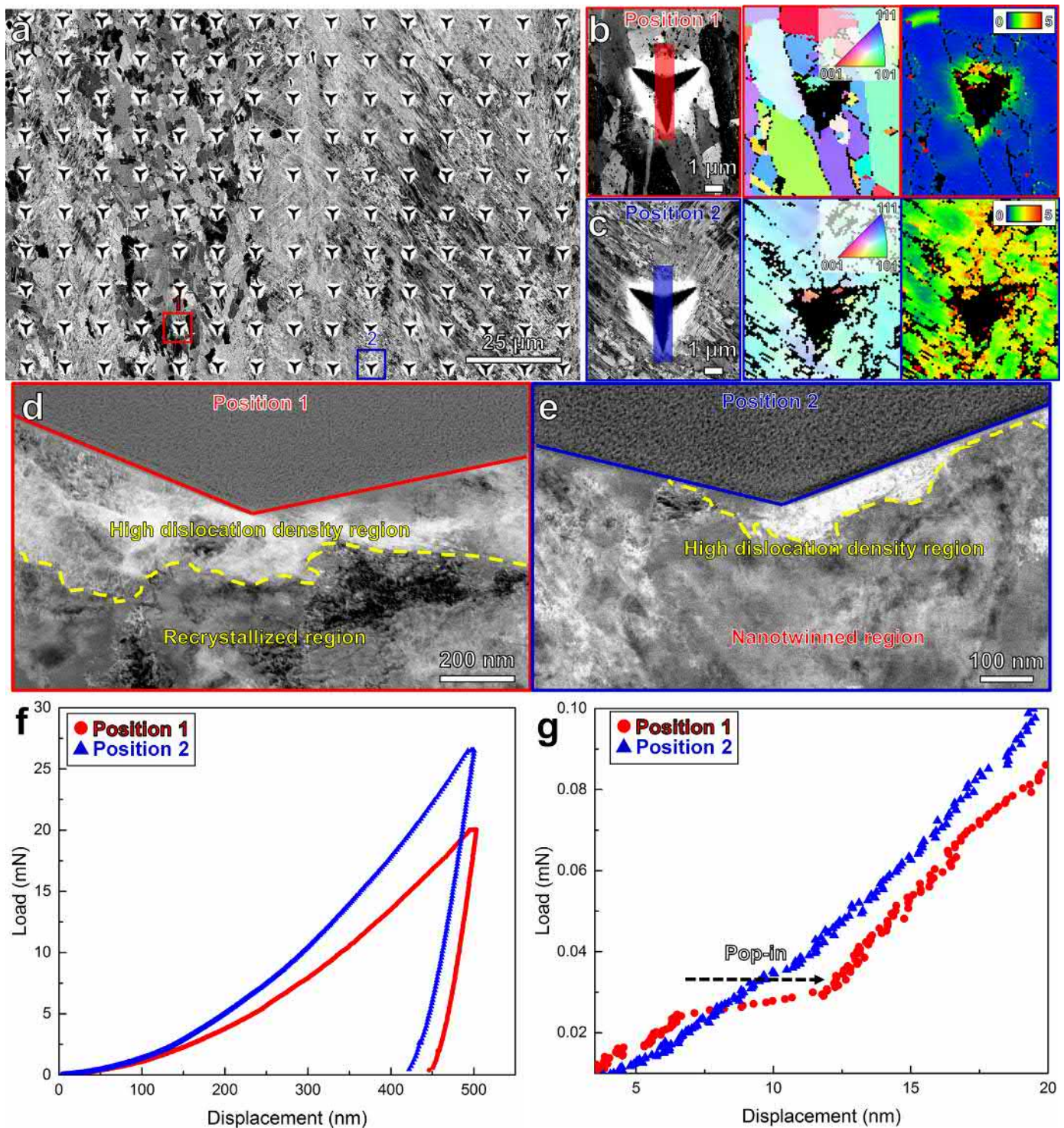


Fig. 9. Typical ECCI and STEM analysis of the sample region in the 900 °C/10 min annealed iHEA probed by nanoindentation. (a) The distribution of indents with a maximum displacement of 500 nm. (b) and (c) are the high-magnification ECCI and EBSD analysis results for positions 1 (the recrystallized region) and 2 (the nanotwinned region), respectively. (d) and (e) are the corresponding cross-sectional LAADF-STEM images for positions 1 and 2, respectively. (f) Two sets of load-displacement curves for the indents of positions 1 and 2. (g) Magnified view of load-displacement curves of (f) shows the “pop-in” behavior in the recrystallized region (position 1) and “continuous” behavior in the nanotwinned region (position 2) at the initial stage of nanoindentation measurement.

formed and the results are displayed in Fig. 9b and c, respectively. The nanoindent at position 1 only covered few grains (Fig. 9b), whereas multiple twin boundaries were included by the nanoindent at position 2 (Fig. 9c). The strain field (i.e., high dislocation density area) caused by the nanoindent can be observed at position 1 (~400 nm, Fig. 9b), revealed by the corresponding KAM

map, but is hardly visible at position 2. This is because the pre-existing dislocation density at position 1 (recrystallized) is much lower than that at position 2 (nanotwinned). To confirm this effect, cross-sectional LAADF-STEM analysis of the materials around the two nanoindents from positions 1 and 2 was conducted and the results are shown in Fig. 9d and e, respectively. It is confirmed

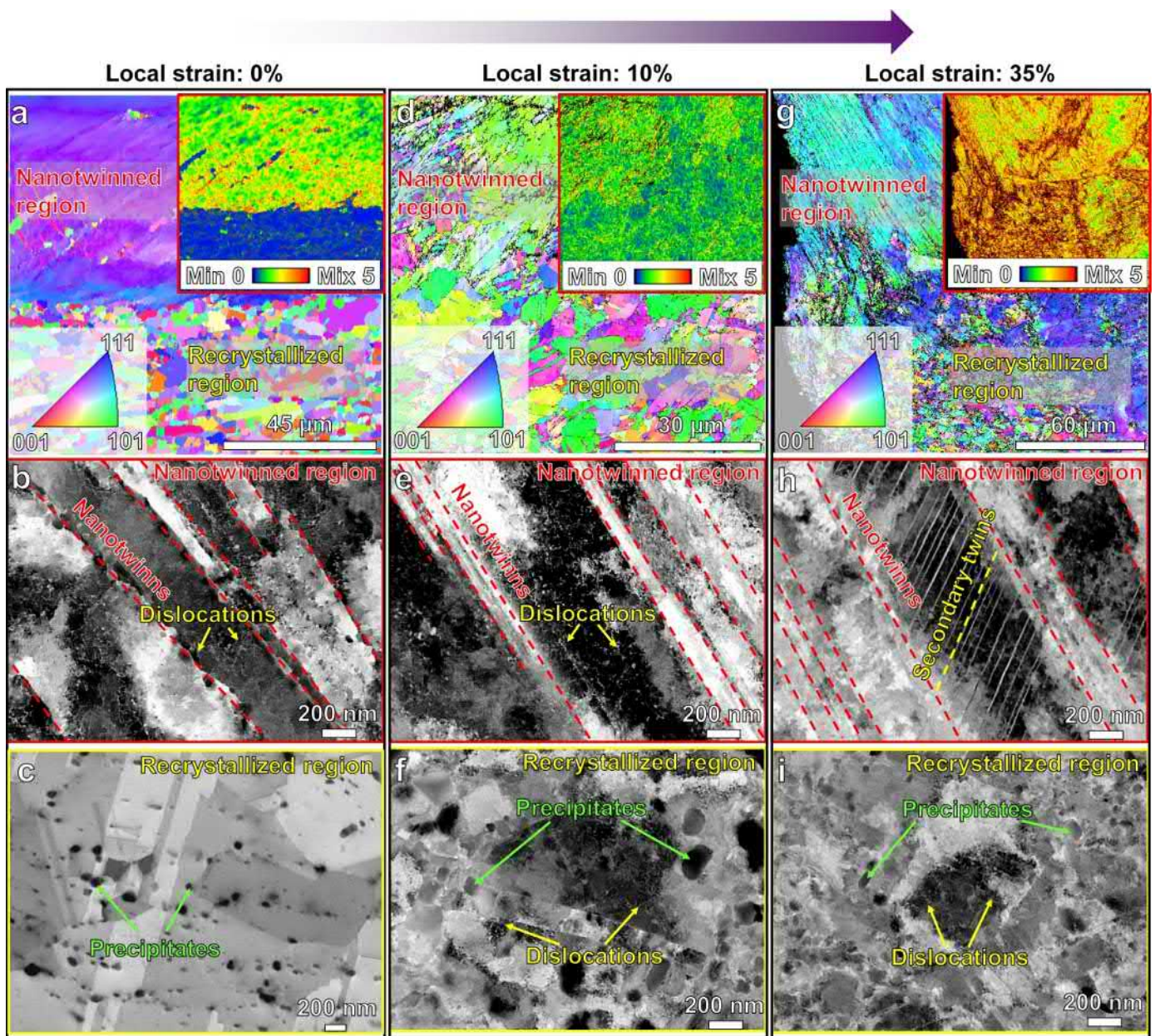


Fig. 10. Deformation microstructures in the nanotwinned iHEA after 900 °C/10 min annealing and tensile testing. Representative EBSD (a, d, g), and ECCE (b–c), (e–f), (h–i), analysis showing the microstructure evolution of both the recrystallized and the nanotwinned regions with increasing local strain: (a–c) local strain of 0%, (d–f) local strain of 10% and (g–i) local strain of 35%.

that the high dislocation density area induced by the nanoindentation at position 1 (~330 nm in depth) was larger than that at position 2 (~80 nm in depth). Prior to indentation, the recrystallized region (e.g., position 1) has lower dislocation density, due to recrystallization, while in the nanotwinned region (e.g., position 2) twin boundaries act as strong barriers for dislocation motion. Also, two representative sets of load-displacement curves corresponding to the indents at positions 1 and 2 are shown in Fig. 9f and g. The maximum loading force taken at position 1 was ~20 mN, i.e. significantly lower than that probed at position 2 (~26.5 mN) at the same maximum displacement, suggesting that the material at position 2 is much harder. The load-displacement curve at position 2 documents a “continuous” response while that at position 1 exhibits a “pop-in” feature at a displacement range of 7 to 12 nm (Fig. 9g). This effect was also reported in previous studies [31], namely, that “pop-in” occurs in regions with low disloca-

tion density (e.g., the recrystallized region at position 1), due to the abrupt formation of entirely new dislocation loops, whereas “continuous” deformation was observed in zones of high dislocation density (e.g., the nanotwinned region of position 2), due to conventional Frank-Read dislocation multiplication.

Compared to the interstitial-free HEA with a hardness value of ~3.2 GPa after 900 °C/10 min annealing, the nanotwinned iHEA exhibits a 72% higher hardness under the same condition (~5.5 GPa) (Fig. 1g). This latter hardness value of the iHEA exceeds those reported for other nanotwinned metals such as 316 L stainless steel [31], Ag [32] and Cu [33] after annealing at 900 °C. This can be mainly attributed to lattice friction (related to solid solution hardening), nanotwins, elongated nano- $M_{23}C_6$ (M: Fe, Mn, Co, Ni and Cr) precipitates and dislocations [34]. The lattice friction stress (σ_0) is estimated to be ~125 MPa [35]. After cold-rolling and annealing, the associated change in lattice friction is assumed to be

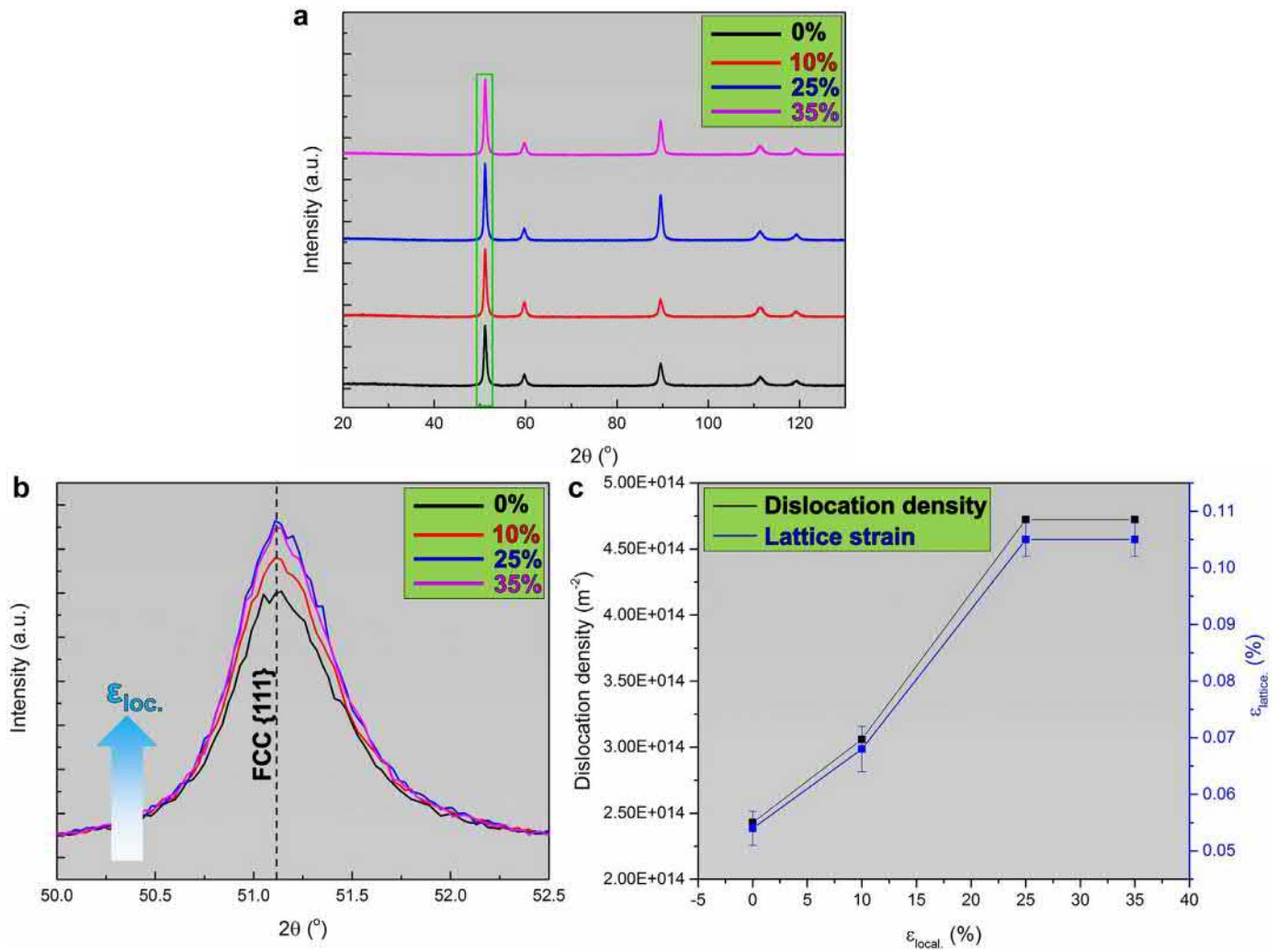


Fig. 11. XRD analysis of the annealed iHEA after tensile deformation. (a) XRD profiles of the deformed iHEA with different tensile straining. (b, c) The broadening of the $\{111\}$ peak indicates an increased microstrains within the matrix after deformation, which is mainly due to the increase of dislocation density.

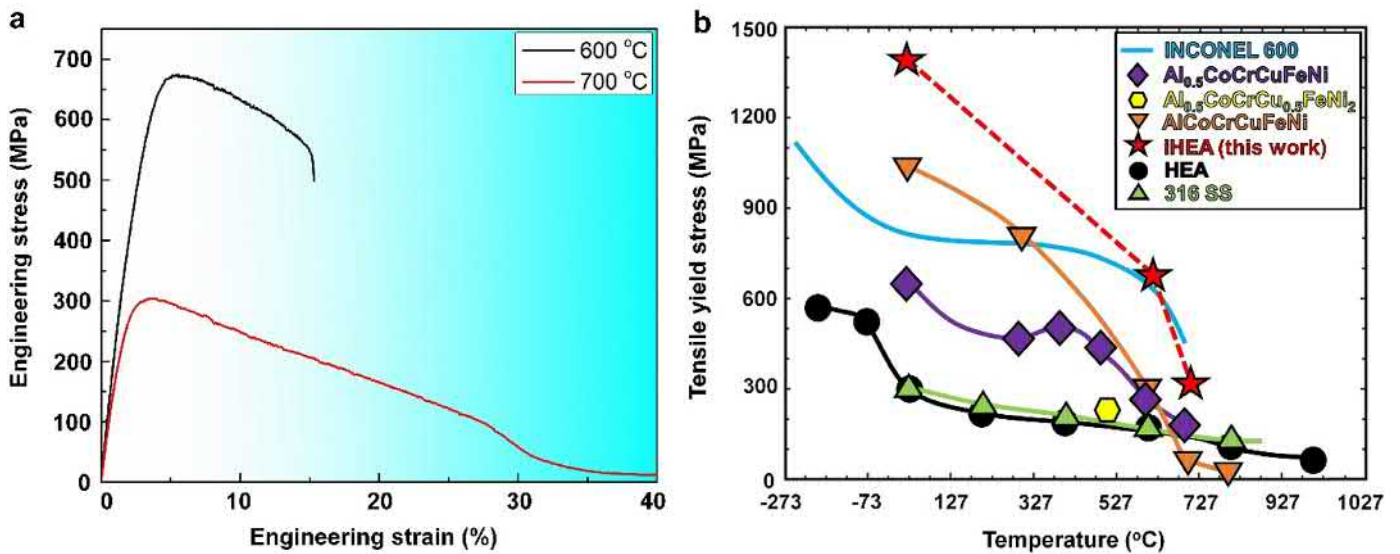


Fig. 12. High temperature tensile data. (a) Engineering stress-strain curves of the nanotwinned iHEA (cold-rolled) at 600 °C and 700 °C. (b) Tensile yield strength as a function of testing temperature for high-temperature engineering alloys including nanotwinned iHEA, CoCrFeMnNi HEA, INCONEL 600, Al_{0.5}CoCrCuFeNi, Al_{0.5}CoCrCu_{0.5}FeNi₂, AlCoCrCuFeNi, and 316 stainless steel [47–50].

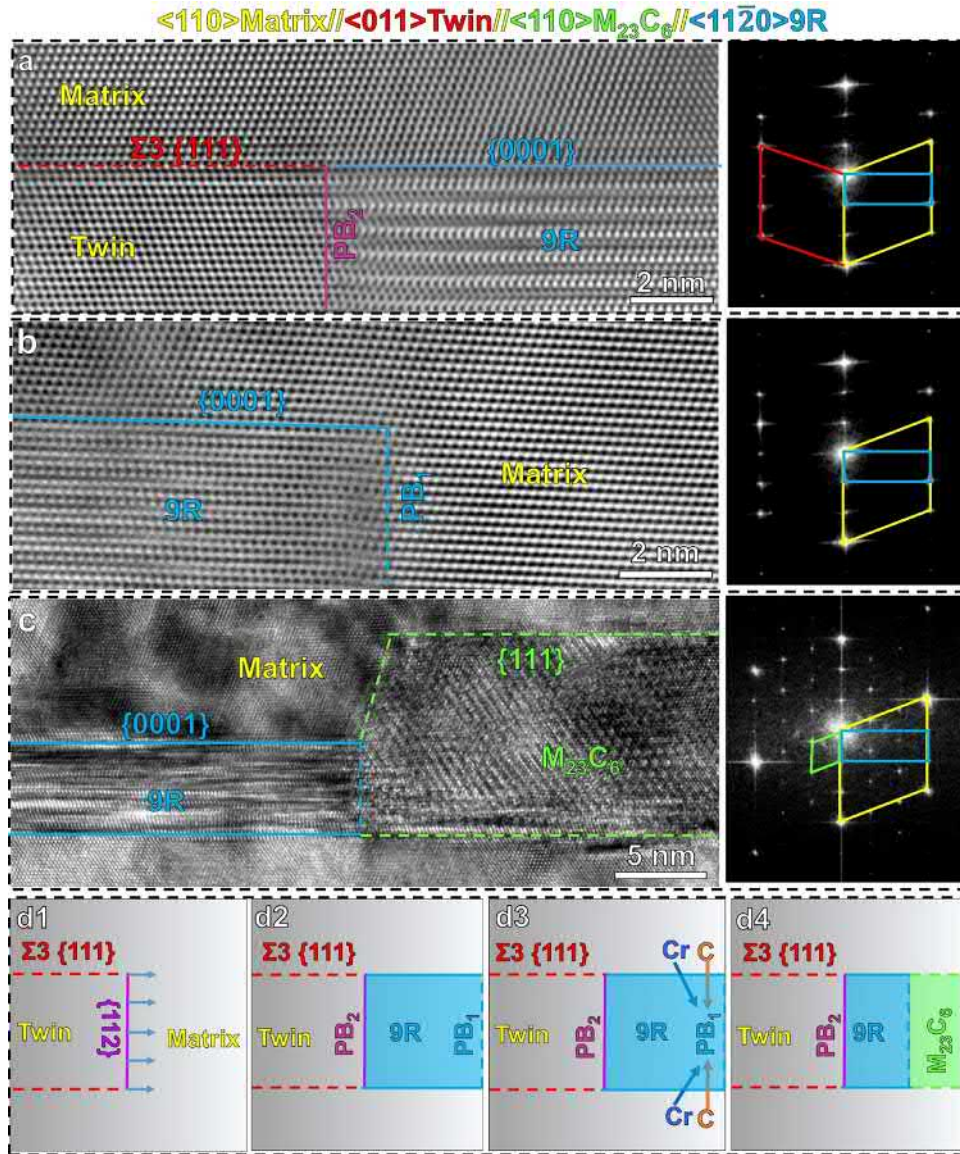


Fig. 13. High-resolution STEM-TEM analysis revealing the formation of nanophases in the nanotwinned iHEA. (a) A representative HAADF-STEM image of the incoherent twin boundary with a 9R structure and PB_2 prior to annealing. (b) Representative STEM image of PB_1 and 9R structure taken from a different location in the specimen prior to annealing. (c) HRTEM view of the elongated $M_{23}C_6$ nano-carbide at PB_1 of the 9R structure after annealing. The corresponding FFT images are displayed below the respective TEM graphs. (d1–d4) Schematic diagrams showing the corresponding sequence of the formation of nanophases: (d1) formation of incoherent twin boundary caused by de-twinning; (d2) formation of 9R structure by motion of b_1 partial dislocations from the incoherent twin boundary; (d3) diffusion process of the interstitial C atoms and the substitutional Cr atoms from the matrix to the newly formed 9R structure; (d4) nucleation of the elongated $M_{23}C_6$ nano-carbide at the phase boundaries of the 9R structure parallel to $\{111\}/\{0001\}$ habit planes and adjacent to the nanotwin boundary. The coherent twin boundary, 9R phase boundary 1 and 9R phase boundary 2 are labeled with “ $\Sigma 3$ ”, “ PB_1 ” and “ PB_2 ”, respectively.

of minor influence and hence ignored during the following estimation. Other factors such as the presence of nanotwins ($\sigma_{nanotwin}$), nano- $M_{23}C_6$ precipitates ($\sigma_{precipitation}$) and dislocations ($\sigma_{dislocation}$) significantly contribute to the increase of the total hardness value after these processing steps. A simple assumption of the different contributions to the total yield strength/hardness can be expressed as:

$$\sigma_{NT} = \sigma_0 + \sigma_{nanotwin} + \sigma_{precipitation} + \sigma_{dislocation} \quad (1)$$

Nanotwin boundaries are an important class of planar and highly coherent barriers that effectively resist dislocation motion in the annealed iHEA [36]. The contribution of the nanotwins to strength follows [4]:

$$\sigma_{nanotwin} = kd^{-\frac{1}{2}} \quad (2)$$

where k is the strengthening coefficient (400–494 MPa $\mu m^{1/2}$) [35,37] and d is the average thickness of the nanotwins (~ 100 nm). Accordingly, the contribution from nanotwins is estimated to be 1265–1562 MPa.

Based on Figs. 1 and 2, a large amount of elongated $M_{23}C_6$ carbides (~ 0.8 vol.%) with an average size of ~ 31 nm was heterogeneously distributed in the nanotwinned region, providing precipitation strengthening. The precipitates are bypassed by dislocations (Orowan-type) when they are incoherent, and they are sheared when they are coherent such as the kappa carbides in the high-Mn lightweight steels [38]. In this work, the Orowan-type precipitation strengthening is expected to dominate since the interface between the elongated $M_{23}C_6$ carbide and the FCC matrix is incoherent [39], as evidenced in Fig. 2. According to the Ashby-Orowan model, the precipitation strengthening of the elongated $M_{23}C_6$ carbides can be

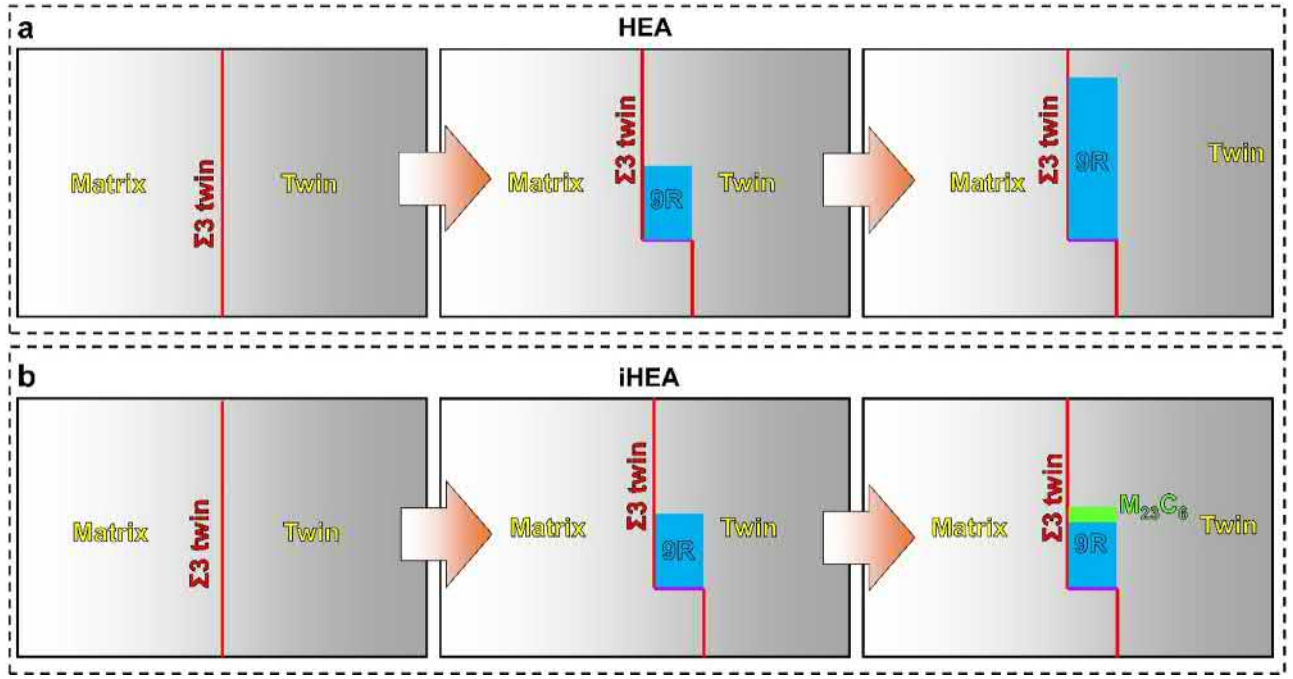


Fig. 14. Schematic diagrams illustrating the de-twinning process. (a) The equiatomic FeMnCoCrNi HEA and (b) iHEA during annealing. The twin boundaries are labelled with “Σ3”.

expressed as [34]:

$$\sigma_{precipitation} = \left(\frac{0.538 G b f^{\frac{1}{2}}}{x} \right) \ln \left(\frac{x}{2b} \right) \quad (3)$$

where G is the shear modulus for the iHEA, b is the magnitude of the Burgers vector, f is the volume fraction of the elongated $M_{23}C_6$ carbides (~0.8 vol.%) and x is the average size of the $M_{23}C_6$ carbides (~31 nm). The shear modulus G is estimated to be ~92 GPa based on the elastic modulus (~238 GPa) measured by nanoindentation (Fig. 8). From the TEM data (Figs. 2 and 4), the Burgers vector b is determined to be ~0.25 nm. Based on Eq. (3), the precipitation hardening contributed by the elongated $M_{23}C_6$ carbides is ~147 MPa.

The high dislocation density in the nanotwinned region of the iHEA (Fig. 10) also contributes to the high hardness. Based on the Bailey-Hirsch formula [5, 34,40,41], the strength provided by a dislocation forest follows:

$$\sigma_{dislocation} = M\alpha Gb\rho^{\frac{1}{2}} \quad (4)$$

where M is the Taylor factor for FCC materials with random texture (3.06), α is a geometry constant (0.2) and ρ is the total dislocation density. The dislocation density can be roughly estimated by the broadening of the XRD diffraction peaks (Fig. 11) via the Williamson-Hall method [40,41]:

$$\rho = 2\sqrt{3} \frac{\epsilon^2}{db} \quad (5)$$

where ϵ is the microstrain caused by dislocations (0.105%) and d is the average grain size (~100 nm). According to Eqs. (4) and (5), the strength contribution from dislocations is ~167 MPa. The total hardness then is approximated to be 5.1–6.0 GPa, i.e., close to the experimentally observed value (~5.5 GPa). This result suggests that the stabilized nanotwins provide the primary contribution to the very high hardness of the iHEA after high-temperature heat-treatment. It is important to note that these nanotwins in the current iHEA can also be stabilized for extended time intervals at elevated temperatures, sustaining the high hardness correspondingly, as shown for specimens heat treated at 800 °C for 60 min

(~6.25 GPa), 800 °C for 300 min (~6 GPa) and 900 °C for 60 min (~4.46 GPa) (Figs. 1g, 6 and 7).

3.3. Tensile deformation at room and high temperatures

Beyond its high hardness, the nanotwinned iHEA after exposure to a 900 °C/10 min annealing treatment (curve 2) has also an excellent combination of yield strength (~1.1 GPa) and ductility (~21%) compared to the as-cold-rolled iHEA (curve 1) (~1.4 GPa and ~1%) and the annealed interstitial-free HEA without nanotwins (curve 3) when exposed to the same processing conditions (0.35 GPa and ~61%) (Fig. 1h). Fig. 1h compares the mechanical properties of the nanotwinned iHEA with those of several key engineering alloys including advanced steels [19]. The comparison shows that the nanotwinned iHEA, when annealed at 900 °C for 10 min, has an excellent combination of ultimate tensile strength (~1.25 GPa) and ductility (~21%), exceeding the values of most advanced reference materials. Such optimized mechanical properties are related to the heterogeneous microstructure of the nanotwinned iHEA (Fig. 1) [26,42,43]. Fig. 10a–c show that both the nanotwinned and recrystallized regions contain pre-existing dislocations and primary twins prior to tensile testing. At local strains up to 35%, secondary twins form within the primary twins in the nanotwinned regions (Fig. 10h). On the other hand, dislocation motion and multiplication prevail in the recrystallized zones (Fig. 10f and i). The increase in dislocation density in the bulk material after tensile testing is confirmed by XRD peak broadening (Fig. 11). This suggests that dislocation plasticity in the twin confined regions accommodates deformation and compensates for misfit in the nanotwinned iHEA [44,45]. We further approximate the tensile strength of the iHEA based on a linear rule-of-mixture [46]:

$$\sigma_T = \sigma_{NT} f_{NT} + \sigma_R f_R \quad (6)$$

where f_{NT} is the volume fraction of the nanotwinned regions (~60 vol.%), σ_{NT} is the strength of the nanotwinned regions (~1700–2000 MPa), f_R is the volume fraction of the recrystallized regions (~40 vol.%) and σ_R is the strength of the recrystallized regions. For the recrystallized regions, σ_R can be expressed as [34]:

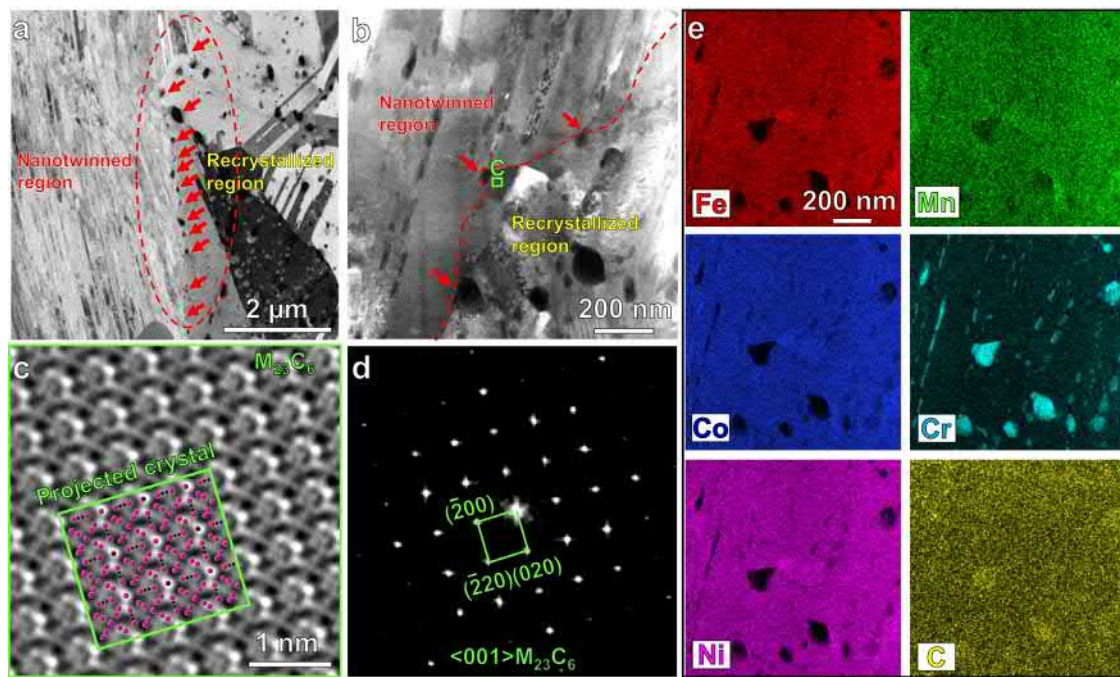


Fig. 15. ECCI-STEM analysis of the boundary area between the nanotwinned and the recrystallized regions of the annealed iHEA. Typical spherical precipitates are characterized by (a) ECCI and (b) HAADF-STEM. The red arrows correspond to the spherical precipitates nucleated at the boundary region marked by red dashed line. (c) A high-resolution HAADF-STEM image of the squared region in (b) showing the spherical precipitate overlaid with the projected crystal of $M_{23}C_6$ along $\langle 001 \rangle$ electron beam direction. (d) The corresponding fast Fourier transform of (c). (e) STEM-EDS mapping of the sample region in (b). (For interpretation of the references to colour in this figure legend, the reader is referred to the web version of this article.)

$$\sigma_R = \sigma_0 + \sigma_{\text{coarse grain}} + \sigma_{\text{round-precipitation}} \quad (7)$$

where $\sigma_{\text{coarse grain}}$ is estimated to be 283–350 MPa through the Hall-Petch effect and $\sigma_{\text{round-precipitation}}$ is approximated as ~67 MPa, using Eq. (3). The total tensile strength (σ_T) then amounts to 1.2–1.4 GPa. The slight discrepancy between the values from this calculation (1.2–1.4 GPa) and the experiments (~1.1 GPa) is attributed to the orientation of the nanotwins inside the sample and the inherent approximations of the rule-of-mixture [46]. As the mechanical response arising from the presence of nanotwins is sensitive to their orientation relative to the loading axis, theoretical maximum and minimum strength limits occur for cases of perpendicular and 45° alignment to the load axis, according to the respective Schmid factors [46].

In addition to the excellent room temperature mechanical properties that are maintained after the described high-temperature processes and service-related heat-treatments, the high thermal stability of the nanotwins in the iHEA leads to a considerable yield strength (670 MPa) and ductility (16%) even at temperatures as high as 600 °C. These values are comparable or even superior to those of some other high-temperature engineering alloys including the INCONEL 600 Ni based superalloy (Fig. 12) [47–50].

3.4. Mechanisms for the formation of elongated carbides and the stabilization of nanotwins

It is worth noting that the elongated precipitate-like regions occur only along the twin boundaries in the nanotwinned regions (Fig. 2a–f), which is essentially different from the spherical carbides in the recrystallized regions (Fig. 4a–f) and the round-shaped precipitates at coherent twin boundaries reported in literature [51–53]. Prior to this observation, $M_{23}C_6$ nano-carbides were not assumed to form at twin boundaries owing to their low solute decoration and low interfacial energy [7,8]. Here, we instead

interpret this phenomenon in terms of a nanoscale 9R phase assisted nano-carbide formation, i.e., an interface stabilized elongated nano-carbide structure in an iHEA, which in turn stabilizes the nanotwins, as will be outlined in detail below.

Fig. 13 provides an overview of the evolution sequence of these interface-aligned nano-carbide zones. First, we observe the formation of incoherent twin boundary portions with hexagonal 9R structure during cold-rolling [14,17–19]. Subsequently, elongated $M_{23}C_6$ nano-carbide zones form at the incoherent segments of the twin interfaces upon annealing as captured by high-resolution STEM/TEM analysis. Energetically, incoherent twin boundary portions are less stable than coherent twin boundaries [54,55]. Upon cold-rolling, the 9R structure initially forms at $\{112\}$ incoherent twin boundary segments and then grows along the $\{111\}$ coherent twin boundary (Fig. 13a, b, d1 and d2), as confirmed by the fast Fourier transform (FFT) analysis shown in Fig. 13a and b. Growth of the 9R structure is promoted by the motion of b_1 edge partial dislocations [17,18] without chemical diffusion. Since the 9R structure with PB_1 (i.e., a set of b_1 partial dislocations, see Fig. 13b) is only formed at the incoherent parts of the nanotwin interfaces, both interstitial C and substitutional Cr can readily co-segregate to these regions. Through this structural-chemical interface stabilization effect, elongated $M_{23}C_6$ nano-carbide zones can form along the $\{111\}_{\text{nanotwin}}//\{0001\}_{9R}$ habit planes upon annealing (Fig. 13c, d3 and d4). This coupled allotropic transformation (FCC to 9R), segregation (C–Cr enrichment at 9R zones) and precipitation (elongated nano-carbides) sequence at the twin interfaces is driven by the relatively high Gibbs free energy of the 9R structure (e.g., 357–484 $\text{mJ}\cdot\text{m}^{-2}$ in Al and 590–714 $\text{mJ}\cdot\text{m}^{-2}$ in Cu) [17–19]. In this process the incoherent parts of the twin boundaries can promote diffusion of Cr and C atoms during annealing [56,57], as revealed by APT analysis (Fig. 2h). It is also worth noting that PB_1 (a set of b_1 edge partial dislocations) of the 9R structure (Fig. 13d4) [17,18] has higher tendency to promote the nucleation of nano-carbides during annealing compared to PB_2 (a set of b_2 and b_3 partial screw

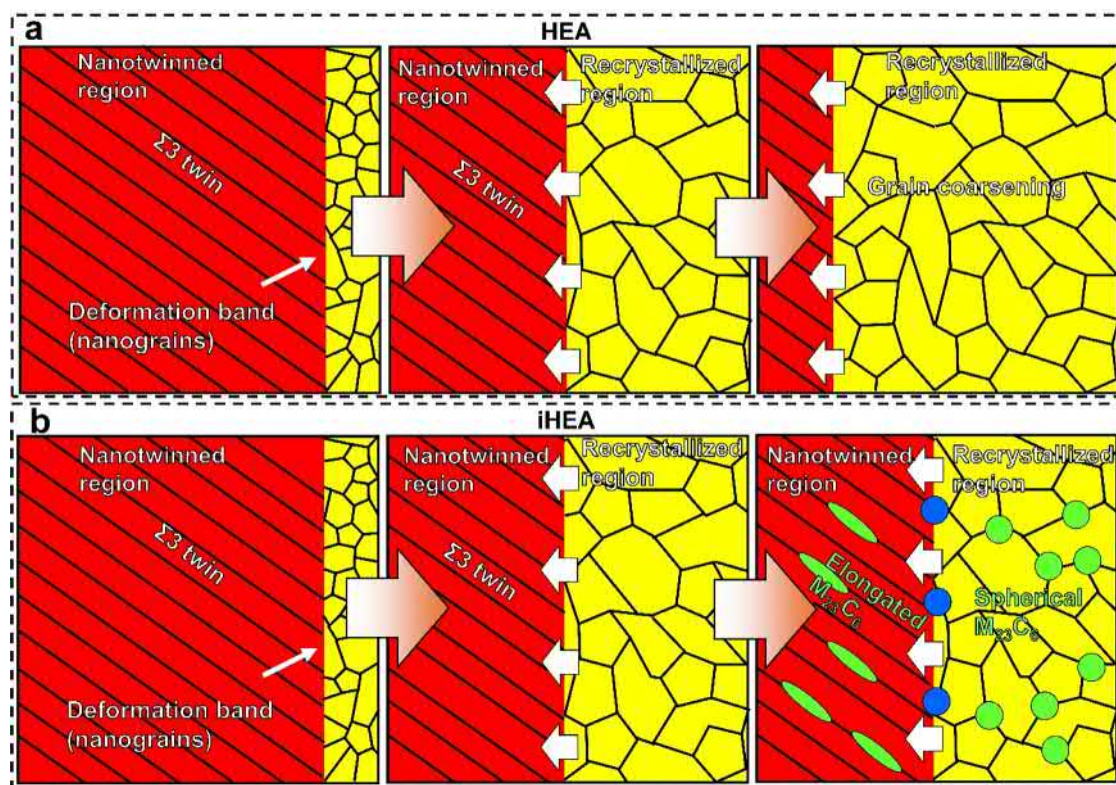


Fig. 16. Schematic diagrams showing the recrystallization process during annealing. (a) Equiatomic FeMnCoCrNi HEA; (b) iHEA. The spherical $M_{23}C_6$ carbides which were observed between the recrystallized and nanotwinned regions in the iHEA can slow down the shrinkage of the nanotwinned region due to Zener pinning. The blue balls in (b) represent the spherical $M_{23}C_6$ carbides. The twin boundaries are labelled with “ $\Sigma 3$ ”. (For interpretation of the references to colour in this figure legend, the reader is referred to the web version of this article.)

dislocations). This is due to the fact that the edge dislocations (PB_1) have larger dislocation excess volume and higher intersection energy than the screw dislocations (PB_2) to promote solutes segregation and sequent precipitation [58,59]. As the elongated $M_{23}C_6$ precipitates form over the 9R structure, the edge dislocations at prior PB_1 vanish (Fig. 13c), preventing the growth of the 9R phase. The formation mechanism of the elongated $M_{23}C_6$ precipitates, revealed above, is substantially different from that of other types of round-shaped precipitates reported in literature, e.g., B2 precipitates at annealing twin boundaries [51–53]. The previously observed precipitates (e.g., B2 and $L1_2$) usually form at dislocations in coherent twin boundaries [51–53]. However, in this work the elongated $M_{23}C_6$ carbides nucleate at the 9R structure, which formed as a result of de-twinning at incoherent twin boundaries. These 9R assisted elongated carbides further hinder the de-twinning process and thereby stabilize the nanotwins at high-temperatures (Fig. 14).

These interfacial nanoscale 9R phases assisted nano-carbides act as twin boundary pinning sites and thus affect their migration and de-twinning, which stabilizes the nano-twins even up to temperatures as high as 900 °C (Fig. 14). Also, the spherical $M_{23}C_6$ carbides (Fig. 15) which were observed between the recrystallized and nanotwinned regions, can slow down shrinkage of nanotwinned regions due to Zener pinning [60,61], as schematically illustrated in Fig. 16. Both types of nano-carbides observed here in the iHEA do not exist in the equiatomic CoCrFeMnNi HEA (Fig. 16).

4. Conclusions

In summary, the interfacial nanophase design strategy – involving the formation of 9R phases and elongated nano-carbides in this work – leads to an unprecedented nanotwin stability, which significantly contributes to the high strength of the iHEA

material. This provides an approach for overcoming the trade-off between strength and thermal stability of nanotwinned materials. We suggest that the same or related interfacial nanophases may generally serve to stabilize nano-twins in a wide range of alloys. The interfacial nanophase design strategy we suggest is achieved by co-segregation of Cr and C to nanoscale 9R structures adjacent to incoherent nanotwin boundaries in the current material. This approach is enabled by simple C doping and it is amenable to conventional bulk metallurgical processing, suggesting that the mechanism can be readily generalized also in other interstitial alloys. This might qualify interstitially alloyed materials with well-tuned interfacial nanophases as a promising pathway for developing strong, ductile and thermally stable bulk nanotwinned materials. We also suggest that interfacial nanophases other than 9R or carbides can be utilized to stabilize nanotwins in other alloys.

Acknowledgements

This work is financially supported by the Deutsche Forschungsgemeinschaft (SPP 2006). Z.L. would like to acknowledge the financial support from the National Science Foundation of China (Grant No. 51971248).

References

- [1] X.C. Liu, H.W. Zhang, K. Lu, Strain-induced ultrahard and ultrastable nanolaminated structure in nickel, *Science* 342 (2013) 3377–340.
- [2] V.Y. Gertsman, R. Birringer, On the room-temperature grain growth in nanocrystalline copper, *Scr. Mater.* 30 (1994) 557–581.
- [3] K. Lu, Stabilizing nanostructures in metals using grain and twin boundary architectures, *Nature Rev. Mater.* 1 (5) (2016).
- [4] F.K. Yan, G.Z. Liu, N.R. Tao, K. Lu, Strength and ductility of 316L austenitic stainless steel strengthened by nano-scale twin bundles, *Acta Mater.* 60 (3) (2012) 1059–1071.

- [5] B.B. Zhang, F.K. Yan, M.J. Zhao, N.R. Tao, K. Lu, Combined strengthening from nanotwins and nanoprecipitates in an iron-based superalloy, *Acta Mater.* 151 (2018) 310–320.
- [6] K. Lu, L. Lu, S. Suresh, Strengthening materials by engineering coherent internal boundaries at the nanoscale, *Science* 324 (2009) 349–352.
- [7] M. Herbig, D. Raabe, Y.J. Li, P. Choi, S. Zaefferer, S. Goto, Atomic-scale quantification of grain boundary segregation in nanocrystalline material, *Phys. Rev. Lett.* 112 (12) (2014) 126103.
- [8] M. Herbig, M. Kuzmina, C. Haase, R.K.W. Marceau, I. Gutierrez-Urrutia, D. Haley, D.A. Molodov, P. Choi, D. Raabe, Grain boundary segregation in Fe–Mn–C twinning-induced plasticity steels studied by correlative electron backscatter diffraction and atom probe tomography, *Acta Mater.* 83 (2015) 37–47.
- [9] V. Randle, ‘Special’ boundaries and grain boundary plane engineering, *Scr. Mater.* 54 (6) (2006) 1011–1015.
- [10] H.K.D.H. Bhadeshia, R.W.K. Honeycombe, *Steels Microstructure and Properties*, 3rd ed., Elsevier, 2005.
- [11] P.H. Pumphrey, H. Gleiter, The annealing of dislocations in high-angle grain boundaries, *Philosoph. Mag.* 30 (1974) 593–602.
- [12] D.G. Brandon, The structure of high-angle grain boundaries, *Acta Mater.* 14 (1966) 1479–1484.
- [13] F. Ernst, M.W. Finnis, D. Hofmann, T. Muschik, U. Schonberger, U. Wolf, M. Methessel, Theoretical prediction and direct observation of the 9R structure in Ag, *Phys. Rev. Lett.* 69 (1992) 620.
- [14] D.L. Medlin, G.H. Campbell, C.B. Carter, Stacking defects in the 9R phase at an incoherent twin boundary in copper, *Acta Mater.* 46 (1998) 5135–5142.
- [15] D.L. Medlin, S.M. Foiles, D. Cohen, A dislocation-based description of grain boundary dissociation: application to a 90 degree $\langle 110 \rangle$ tilt boundary in gold, *Acta Mater.* 49 (2001) 3689–3697.
- [16] J.A. Brown, N.M. Ghoniem, Structure and motion of junctions between coherent and incoherent twin boundaries in copper, *Acta Mater.* 57 (2009) 4454–4462.
- [17] J. Wang, O. Anderoglu, J.P. Hirth, A. Misra, X. Zhang, Dislocation structures of $\Sigma 3$ {112} twin boundaries in face centered cubic metals, *Appl. Phys. Lett.* 95 (2) (2009) 021908.
- [18] L. Liu, J. Wang, S.K. Gong, S.X. Mao, High resolution transmission electron microscope observation of zero-strain deformation twinning mechanisms in Ag, *Phys. Rev. Lett.* 106 (17) (2011) 175504.
- [19] J. Wang, B. Liu, C.T. Liu, Y. Liu, Strengthening mechanism in a high-strength carbon-containing powder metallurgical high entropy alloy, *Intermetallics* 102 (2018) 58–64.
- [20] M. Kuzmina, M. Herbig, D. Ponge, S. Sandlobes, D. Raabe, Linear complexions: confined chemical and structural states at dislocations, *Science* 349 (2015) 1080–1083.
- [21] W.C. Oliver, G.M. Pharr, Measurement of hardness and elastic modulus by instrumented indentation: advances in understanding and refinements to methodology, *J. Mater. Res.* 19 (01) (2011) 3–20.
- [22] W. Lu, C.H. Liebscher, G. Dehm, D. Raabe, Z. Li, Bidirectional transformation enables hierarchical nanolaminate dual-phase high-entropy alloys, *Adv. Mater.* (2018) 1804727.
- [23] W. Lu, M. Herbig, C.H. Liebscher, L. Morsdorf, R.K.W. Marceau, G. Dehm, D. Raabe, Formation of eta carbide in ferrous martensite by room temperature aging, *Acta Mater.* 158 (2018) 297–312.
- [24] F.S. Li, J.B. Yang, D.S. Xue, R.J. Zhou, X-ray diffraction and mossbauer studies of the $(\text{Fe}_{1-x}\text{Ni}_x)_4\text{N}$ compounds ($0 \leq x \leq 0.5$), *J. Magn. Magn. Mater.* 151 (1995) 221–224.
- [25] H.L. Yakel, Atom distributions in tau-carbide phases: Fe and Cr distributions in $(\text{Cr}_{23-x}\text{Fe}_x)\text{C}_6$ with $x = 0, 0.74, 1.70, 4.13$ and 7.36 , *Acta Crystal. B* 43 (1987) 230–238.
- [26] X. Wu, M. Yang, F. Yuan, G. Wu, Y. Wei, X. Huang, Y. Zhu, Heterogeneous lamella structure unites ultrafine-grain strength with coarse-grain ductility, *Proc. Natl. Acad. Sci. U.S.A.* 112 (47) (2015) 14501–14505.
- [27] X. Li, K. Lu, Playing with defects in metals, *Nat. Mater.* 16 (7) (2017) 700–701.
- [28] J.-K. Du, C.-H. Wang, K.-C. Wang, K.-K. Chen, TEM analysis of 2205 duplex stainless steel to determine orientation relationship between M_{23}C_6 carbide and austenite matrix at 950°C, *Intermetallics* 45 (2014) 80–83.
- [29] Z. Xu, Z. Ding, L. Dong, B. Liang, Characterization of M_{23}C_6 carbides precipitating at grain boundaries in 100Mn13 steel, *Metallurg. Mater. Transact. A* 47 (10) (2016) 4862–4868.
- [30] K. Yamanaka, M. Mori, K. Sato, A. Chiba, Characterisation of nanoscale carbide precipitation in as-cast Co–Cr–W-based dental alloys, *J. Mater. Chem. B* 4 (10) (2016) 1778–1786.
- [31] F.K. Yan, B.B. Zhang, H.T. Wang, N.R. Tao, K. Lu, Nanoindentation characterization of nano-twinned grains in an austenitic stainless steel, *Scr. Mater.* 112 (2016) 19–22.
- [32] D. Bufford, H. Wang, X. Zhang, Thermal stability of twins and strengthening mechanisms in differently oriented epitaxial nanotwinned Ag films, *J. Mater. Res.* 28 (13) (2013) 1729–1739.
- [33] O. Anderoglu, A. Misra, H. Wang, X. Zhang, Thermal stability of sputtered Cu films with nanoscale growth twins, *J. Appl. Phys.* 103 (9) (2008) 094322.
- [34] H. Cheng, H.Y. Wang, Y.C. Xie, Q.H. Tang, P.Q. Dai, Controllable fabrication of a carbide-containing FeCoCrNiMn high-entropy alloy: microstructure and mechanical properties, *Mater. Sci. Technol.* 33 (17) (2017) 2032–2039.
- [35] F. Otto, A. Dlouhy, C. Somsen, H. Bei, G. Eggeler, E.P. George, The influences of temperature and microstructure on the tensile properties of a CoCrFeMnNi high-entropy alloy, *Acta Mater.* 61 (15) (2013) 5743–5755.
- [36] D.R. Steinmetz, T. Jäpel, B. Wietbrock, P. Eisenlohr, I. Gutierrez-Urrutia, A. Saeed-Akbari, T. Hickel, F. Roters, D. Raabe, Revealing the strain-hardening behavior of twinning-induced plasticity steels: theory, simulations, experiments, *Acta Mater.* 61 (2) (2013) 494–510.
- [37] M. Klimova, N. Stepanov, D. Shaysultanov, R. Chernichenko, N. Yurchenko, V. Sanin, S. Zhrebtsov, Microstructure and mechanical properties evolution of the Al, C-Containing CoCrFeMn-type high-entropy alloy during cold rolling, *Materials (Basel)* 11 (1) (2017).
- [38] M. Yao, E. Welsch, D. Ponge, S.M.H. Haghighat, S. Sandlobes, P. Choi, M. Herbig, I. Bleskov, T. Hickel, M. Lipinska-Chwalek, Strengthening and strain hardening mechanisms in a precipitation-hardened high-Mn lightweight steel, *Acta Mater.* 140 (2017) 258–273.
- [39] Q. Wang, Z. Li, S. Pang, X. Li, C. Dong, P.K. Liaw, Coherent precipitation and strengthening in compositionally complex alloys: a review, *Entropy* 20 (11) (2018) 878.
- [40] Y.H. Zhao, H.W. Sheng, K. Lu, Microstructure evolution and thermal properties in nanocrystalline Fe during mechanical attrition, *Acta Mater.* 49 (2001) 365–375.
- [41] G.K. Williamson, R.E. Smallman III, Dislocation densities in some annealed and cold-worked metals from measurements on the X-ray debye-scherrer spectrum, *Philosoph. Mag.* 1 (1) (1956) 34–46.
- [42] J. Li, Y. Ni, A.K. Soh, X. Wu, Strong crack blunting by hierarchical nanotwins in ultrafine/nano-grained metals, *Mater. Res. Lett.* 3 (4) (2015) 190–196.
- [43] J. Li, W. Lu, S. Chen, C. Liu, Revealing extra strengthening and strain hardening in heterogeneous two-phase nanostructures, *Int. J. Plast.* (2019).
- [44] P. Zhou, Z.Y. Liang, R.D. Liu, M.X. Huang, Evolution of dislocations and twins in a strong and ductile nanotwinned steel, *Acta Mater.* 111 (2016) 96–107.
- [45] B.B. He, B. Hu, H.W. Yen, G.J. Cheng, Z.K. Wang, H.W. Luo, M.X. Huang, High dislocation density-induced large ductility in deformed and partitioned steels, *Science* 357 (2017) 1029–1032.
- [46] F. Yan, Q. Li, N. Tao, Anisotropic strengthening of nanotwinned austenitic grains in a nanotwinned stainless steel, *Scr. Mater.* 142 (2018) 15–19.
- [47] C.-W. Tsai, M.-H. Tsai, J.-W. Yeh, C.-C. Yang, Effect of temperature on mechanical properties of Al_{0.5}CoCrCuFeNi wrought alloy, *J. Alloys Compounds* 490 (1–2) (2010) 160–165.
- [48] A. Gali, E.P. George, Tensile properties of high- and medium-entropy alloys, *Intermetallics* 39 (2013) 74–78.
- [49] C. Ng, S. Guo, J. Luan, Q. Wang, J. Lu, S. Shi, C.T. Liu, Phase stability and tensile properties of Co-free Al_{0.5}CrCuFeNi₂ high-entropy alloys, *J. Alloys Compounds* 584 (2014) 530–537.
- [50] D.B. Miracle, O.N. Senkov, A critical review of high entropy alloys and related concepts, *Acta Mater.* 122 (2017) 448–511.
- [51] T.M. Smith, B.D. Esser, N. Antolin, A. Carlsson, R.E. Williams, A. Wessman, T. Hanlon, H.L. Fraser, W. Windl, D.W. McComb, M.J. Mills, Phase transformation strengthening of high-temperature superalloys, *Nat. Commun.* 7 (2016) 13434.
- [52] D. Choudhuri, S. Shukla, W.B. Green, B. Gwalani, V. Ageh, R. Banerjee, R.S. Mishra, Crystallographically degenerate B2 precipitation in a plastically deformed fcc-based complex concentrated alloy, *Mater. Res. Lett.* 6 (3) (2018) 171–177.
- [53] X. Wang, W. Zhou, P. Liu, S. Song, K.M. Reddy, Atomic scale structural characterization of B2 phase precipitated along fcc twin boundary in a CoCrFeNi_{0.3} high entropy alloy, *Scr. Mater.* 162 (2019) 161–165.
- [54] X. Zhou, X.X. Yu, T. Kaub, R.L. Martens, G.B. Thompson, Grain boundary specific segregation in nanocrystalline Fe(Cr), *Sci. Rep.* 6 (2016) 34642.
- [55] D. Terentyev, X. He, E. Zhurkin, A. Bakaev, Segregation of Cr at tilt grain boundaries in Fe–Cr alloys: a metropolis monte carlo study, *J. Nuclear Mater.* 408 (2011) 161–170.
- [56] L. Wang, J. Teng, D. Kong, G. Yu, J. Zou, Z. Zhang, X. Han, In situ atomistic deformation mechanisms of twin-structured nanocrystal Pt, *Scr. Mater.* 147 (2018) 103–107.
- [57] K.Y. Yu, D. Bufford, C. Sun, Y. Liu, H. Wang, M.A. Kirk, M. Li, X. Zhang, Removal of stacking-fault tetrahedra by twin boundaries in nanotwinned metals, *Nat. Commun.* 4 (2013) 1377.
- [58] Y. Hanlumu, P.A. Gordon, T. Neeraj, D.C. Chrzan, Interactions between carbon solutes and dislocations in bcc iron, *Acta Mater.* 58 (16) (2010) 5481–5490.
- [59] J. Takahashi, K. Kawakami, J.-i. Hamada, K. Kimura, Direct observation of niobium segregation to dislocations in steel, *Acta Mater.* 107 (2016) 415–422.
- [60] H.S. Zurb, C.R. Hutchinson, Y. Brechet, G. Purdy, Modelling recrystallization of microalloyed austenite: effect of coupling recovery, precipitation and recrystallization, *Acta Mater.* 50 (2002) 3075–3092.
- [61] L. Vanherpe, N. Moelans, B. Blanpain, S. Vandewalle, Pinning effect of spheroid second-phase particles on grain growth studied by three-dimensional phase-field simulations, *Comput. Mater. Sci.* 49 (2) (2010) 340–350.